

# CARMA observations of massive *Planck*-discovered cluster candidates at $z \gtrsim 0.5$ associated with *WISE* overdensities: strategy, observations and validation

Carmen Rodríguez-Gonzálvez,<sup>1\*</sup> Stephen Muchovej<sup>2</sup> and Ranga Ram Chary<sup>1</sup>

<sup>1</sup>US Planck Data Center, MS220-6, Pasadena, CA 91125, USA

<sup>2</sup>Owens Valley Radio Observatory, California Institute of Technology, Big Pine, CA 93513, USA

Accepted 2014 November 18. Received 2014 November 17; in original form 2014 May 23

## ABSTRACT

We present 1–2 arcmin spatial resolution Combined Array for Research in Millimetre-wave Astronomy (CARMA)-8 31 GHz observations towards 19 unconfirmed *Planck* cluster candidates, selected to have significant galaxy overdensities from the *WISE* early data release and thought to be at  $z \gtrsim 1$  from the *WISE* colours of the putative brightest cluster galaxy. We find a Sunyaev–Zeldovich (SZ) detection in the CARMA-8 data towards nine candidate clusters, where one detection is considered tentative. For each cluster candidate we present CARMA-8 maps, a study of their radio-source environment and we assess the reliability of the SZ detection. The CARMA SZ detections appear to be SZ bright, with the mean, primary-beam-corrected peak flux density of the decrement being  $-2.9$  mJy beam<sup>-1</sup> with a standard deviation of 0.8, and are typically offset from the *Planck* position by  $\approx 80$  arcsec. Using archival imaging data in the vicinity of the CARMA SZ centroids, we present evidence that one cluster matches Abell 586 – a known  $z \approx 0.2$  cluster; four candidate clusters are likely to have  $0.3 \lesssim z \lesssim 0.7$ ; and, for the remaining four, the redshift information is inconclusive. We also argue that the sensitivity limits resulting from the cross-correlation between *Planck* and *WISE* makes it challenging to use our selection criterion to identify clusters at  $z > 1$ .

**Key words:** galaxies: clusters: general – cosmic background radiation – large-scale structure of Universe – radio continuum: general.

## 1 INTRODUCTION

Galaxy clusters form over a Hubble time from rare, high-density peaks in the primordial density field on scales of a few Mpc. Their assembly via the hierarchical merging of smaller haloes from  $0 < z < 3$  straddles the period of dark energy domination and, on the largest scales, is driven primarily by gravitational physics with little effect from e.g. complex gas dynamics, feedback and stellar mass (see e.g. Bond, Kofman & Pogosyan 1996; Allen, Evrard & Mantz 2011, for a review). As a result, cluster abundance – the number of clusters per comoving volume per solid angle above a certain mass – as a function of redshift depends solely on the expansion history of the Universe and the growth of the initial fluctuations (Bardeen et al. 1986; Bond & Myers 1996). In principle, measuring the evolution of the cluster mass function with redshift provides an independent probe for placing strong constraints on cosmological parameters (e.g. Viana & Liddle 1996; Bahcall & Fan 1998; Voit 2005). However, the ability to extract precision cosmology from

cluster surveys relies on the selection function being well understood and the precise characterization of how a cluster observable translates to a cluster mass.

Lying on the exponential tail of the mass function, the most massive clusters are of particular interest, especially those at high redshifts,  $z$ , as they yield the largest differences between cosmologies. But, identifying such systems has been challenging, since they are inherently rare and since historically clusters have been detected via their optical flux or from the X-ray emission of the hot intracluster medium (ICM; observational methods that suffer from cosmological dimming). In recent years, significant progress in this quest has been made through Sunyaev–Zel’dovich (SZ) surveys like ACT (Marriage et al. 2011), SPT (Williamson et al. 2011) and *Planck* (Planck Collaboration 2011b). When cosmic microwave background (CMB) photons travelling towards us traverse the hot ICM, many are inverse-Compton scattered by the hot electrons in the plasma producing a shift in the blackbody spectrum of the CMB known as the SZ effect (Sunyaev & Zel’dovich 1972; see Carlstrom, Holder & Reese 2002 for a review). The total, or integrated SZ signal,  $Y_{SZ}$ , has been shown to correlate tightly with mass, it is only weakly dependent on redshift at  $z \gtrsim 0.3$  and has a weak bias to gas

\* E-mail: [carmen.rodrig25@gmail.com](mailto:carmen.rodrig25@gmail.com)

concentration (e.g. Motl et al. 2005; Bonaldi et al. 2007; Kay et al. 2012).

The ACT and SPT SZ-cluster surveys cover relatively small areas of sky [ $\approx 500$  sq degree Hasselfield et al. (2013) and  $\approx 2500$  Williamson et al. (2011), respectively] at arcminute resolution with the benefit of probing the low-to-medium mass end of the mass function. These surveys are complementary to the *Planck* mission (Tauber et al. 2010; Planck Collaboration 2011a), which is designed to detect the most massive clusters over the entire sky. The latest *Planck* results based on 15.5 months of data contain measurements towards 1227 systems; 683 of these entries match a known cluster and, out of the 544 newly discovered objects, 178 have been confirmed to be clusters through follow-up observations (Planck Collaboration 2013c). One of the major drawbacks of *Planck* is its spatial resolution, which is between 5 and 10 arcmin at the relevant frequencies, and contributes to the  $\gtrsim 30$  percent errors on cluster parameters (Planck Collaboration 2013a). Thus, to fully exploit the characteristics of *Planck* clusters to constrain cosmology, high-resolution follow-up of the catalogued clusters is necessary.

For this project we have used the eight-element subarray of the Combined Array for Research in Millimetre-wave Astronomy, CARMA-8, to follow up 19 unconfirmed *Planck*-discovered cluster candidates which we believed to be at  $z \gtrsim 1.0$  from their *WISE* colours. Previous high-resolution SZ follow up of *Planck*-detected clusters and candidate clusters has been undertaken by Muchovej et al. (2010), AMI Consortium (2011), Sayers et al. (2012), Planck Collaboration (2013a) and Perrott et al. (2014).

This work is divided into two papers. The first one, presented here, focuses on validating the sample candidate clusters. The second (Rodríguez-González et al., in preparation) aims to constrain cluster parameters by fitting models to the data in a Bayesian Monte Carlo Markov chain framework. The current paper is organized as follows: details on the instruments and target selection are provided in Section 2. The CARMA data, including processing and main results, are presented in Section 3. Validation work using ancillary data sets is described in Section 4. In Section 5 we discuss whether any of the cluster candidates without a CARMA-8 SZ detection are likely to be real. In Section 6, we (1) explore which of the selection criteria correlate best with detectability and (2) make use of *WISE* and Sloan Digital Sky Survey (SDSS) to estimate or place constraints on the cluster redshift. The conclusions drawn from this study are provided in Section 7.

Throughout this work we present images where north (N) is up and east (E) is to the left. We use J2000 coordinates, as well as a  $\Lambda$  cold dark matter cosmology with  $\Omega_m = 0.3$ ,  $\Omega_\Lambda = 0.7$ ,  $\Omega_k = 0$ ,  $\Omega_b = 0.041$ ,  $w_0 = -1$ ,  $w_a = 0$  and  $\sigma_8 = 0.8$ .  $H_0$  is taken as  $70 \text{ km s}^{-1} \text{ Mpc}^{-1}$ .

## 2 CLUSTER SAMPLE

### 2.1 Instruments: CARMA and *Planck*

The CARMA-8 telescope, previously known as the Sunyaev-Zel'dovich Array, is an interferometer operating at 31 GHz comprising eight antennas of 3.5 m in diameter. Six of the antennas are arranged in a compact configuration (with baselines in the range  $\approx 4\text{--}20$  m or  $\sim 0.4\text{--}2 \text{ k}\lambda$ ) to be sensitive to large-scale structure at 1–2 arcmin resolution and the two outliers, with baselines of  $\approx 50$  m or 2–10  $\text{k}\lambda$ , provide the high-resolution data ( $\approx 20$  arcsec) to enable contaminating radio-point sources to be detected and removed accurately. It has a bandwidth of 8 GHz divided into 16 500 MHz channels, a 10.5 arcmin full width at half-maximum (FWHM) primary

beam (PB) and typical system temperatures of 40–50 K. Further details on the instrument can be found in Muchovej et al. (2007). Henceforth, we shall refer to the short-baseline data from the compact subarray (0–2  $\text{k}\lambda$ ) as SB data and to the long-baseline data (2–8  $\text{k}\lambda$ ) as LB data.

The *Planck* satellite (Tauber et al. 2010; Planck Collaboration 2011a) is a third generation space-based mission to study the CMB and foregrounds to the CMB. It has mapped the entire sky at nine frequency bands from 30 to 857 GHz, with angular resolution of 33 to 5 arcmin, respectively. The bands where the SZ decrement is strongest have resolutions of 7–10 arcmin.

### 2.2 Sample selection

The 19 clusters comprising our sample are all candidate clusters detected in the *Planck* all-sky maps; they are listed in Table 1. They were selected by cross-correlating *WISE* early data release<sup>1</sup> and *Planck* catalogues of SZ candidate clusters. The *Planck* SZ catalogue used for the primary selection was an intermediate *Planck* data product known internally as DX7.<sup>2</sup> Candidate clusters were identified in the maps using a matched-filter component separation algorithm, MMF3<sup>3</sup> (Melin et al. 2006). Henceforth, results derived from the MMF3 analysis of *PLANCK* DX7 data will be referred to as *PLANCK* results. We initially searched the *WISE* early data release (Wright et al. 2010) at the location of the *Planck* cluster candidates and estimated a value for the overdensity of *WISE* objects. The average density of *WISE* galaxies detected at 3.4 and 4.6  $\mu\text{m}$  was first calculated within 4.75 arcmin of the *Planck* position and, secondly, within an annulus with a 4.75 arcmin inner radius and a 7 arcmin outer radius.<sup>4</sup> The difference between these two density measurements yields a value for the overdensity of *WISE* objects in the vicinity of each *Planck* cluster candidate (see Fig. 1).

Coarse photometric redshifts were calculated from the [3.4] – [4.6] *WISE* colours of the brightest red object within 2.5 arcmin<sup>5</sup> of the *Planck* position fainter than 15.8 Vega mag at 3.4  $\mu\text{m}$  (which corresponds to a  $10L_*$  galaxy at  $z \approx 1$ <sup>6</sup>). The purpose of the magnitude

<sup>1</sup> At the time when our sample of targets was selected the *WISE* early data release was the most up to date publicly available *WISE* data product.

<sup>2</sup> *Planck* data are collected and reduced in blocks of time. The DX7 all-sky maps used in this analysis correspond to the reduction of *Planck* data collected from 2009 August 12 to 2010 of November 28, which is equivalent to three full all-sky surveys, using the v4.1 processing pipeline. The DX7 maps used in this work are part of an internal release amongst the *Planck* Collaboration members and, thus, is not a publicly available data product. The *Planck* Union catalogue (PSZ) is based on more recent and refined processing of the data, including improved pointing and calibration.

<sup>3</sup> Three algorithms: MMF1 (Herranz et al. 2002), MMF3 (Melin, Bartlett & Delabrouille 2006) and PwS (Carvalho, Rocha & Hobson 2009; Carvalho et al. 2012) have been used to identify cluster candidates from the *Planck* data (see *Planck* Collaboration 2013c).

<sup>4</sup> The choice of 4.75 arcmin as the inner radius is based on the *Planck* beam ( $\approx 9.5$  arcmin at 100 GHz). Although the typical separations between *Planck* and X-ray cluster centroids from the early *Planck* SZ-cluster catalogue (*Planck* Collaboration 2011b) were found to typically be  $\approx 2$  arcmin, we chose a larger radius to avoid introducing selection biases that could arise from picking systems with smaller offsets, which might be in a more relaxed dynamical state. However, from the CARMA-8 results, we find that we only detect systems within  $\lesssim 2.5$  arcmin from the *Planck* position.

<sup>5</sup> For some of the clusters in our sample the brightest red object in *WISE* used to obtain a photometric redshift estimate is  $>2.5$  arcmin from the *Planck* position since earlier versions of the algorithm used to select the cluster sample did not impose such a tight constraint on the radial search.

<sup>6</sup> *WISE* is sensitive to a galaxy mass of  $5 \times 10^{11} M_\odot$  at  $z \approx 1$ .

**Table 1.** Details on the CARMA-8 data. For simplicity and homogeneity in the cluster naming convention we use a shorthand ID for the targets. The PSZ (Union catalogue) name (Planck Collaboration 2013c) is provided, where available<sup>a</sup>. The RA and Dec coordinates correspond to the map centre of our CARMA-8 observations. For the short and long baseline data we provide the ellipse parameters for the synthesized beam and the visibility noise. Targets that have been detected in the CARMA-8 data have their ID highlighted. For P014, the SZ signal in the CARMA-8 data is considered tentative.

Cluster ID	Union name	RA ( <sup>h</sup> <sup>m</sup> <sup>s</sup> )	Dec. ( <sup>°</sup> <sup>'</sup> <sup>''</sup> )	Short baselines (0–2 kλ)			Long baselines (2–8 kλ)		
				Beam (arcsec × arcsec) <sup>b</sup>	Position angle ( <sup>°</sup> )	σ (mJy beam <sup>-1</sup> ) <sup>b</sup>	Beam (arcsec × arcsec) <sup>a</sup>	Position angle ( <sup>°</sup> )	σ (mJy beam <sup>-1</sup> ) <sup>c</sup>
<b>P014</b>	PSZ1G014.13+38.38	16 03 21.62	03 19 12.00	91.4 × 102.2	83.0	0.309	15.7 × 19.5	44.9	0.324
P028	PSZ1G028.66+50.16	15 40 10.15	17 54 25.14	123.8 × 129.9	−37.4	0.433	17.4 × 24.0	64.4	0.451
P031	–	15 27 37.83	20 40 44.28	92.6 × 234.9	−84.5	0.727	16.5 × 28.9	48.0	0.633
P049	–	14 44 21.61	31 14 59.88	108.0 × 158.0	−52.9	0.557	17.5 × 25.0	85.1	0.572
P052	–	21 19 02.42	00 33 00.00	87.4 × 107.5	53.1	0.368	14.7 × 21.0	38.2	0.386
P057	PSZ1G057.71+51.56	15 48 34.13	36 07 53.86	119.7 × 133.9	−41.8	0.451	16.7 × 25.9	88.0	0.482
<b>P086</b>	PSZ1G086.93+53.18	15 13 53.36	52 46 41.56	124.0 × 143.7	70.4	0.622	18.2 × 24.4	54.0	0.599
P090	PSZ1G090.82+44.13	16 03 43.65	59 11 59.61	118.2 × 147.7	−65.0	0.389	19.5 × 24.4	42.7	0.427
<b>P097</b>	–	14 55 13.99	58 51 42.44	115.3 × 169.4	−84.2	0.653	21.0 × 25.0	48.4	0.660
<b>P109</b>	PSZ1G109.88+27.94	18 23 00.19	78 21 52.19	112.3 × 185.0	−86.4	0.562	23.3 × 25.6	−39.1	0.517
P121	PSZ1G121.15+49.64	13 03 26.20	67 25 46.70	82.2 × 193.1	85.4	0.824	21.5 × 23.4	89.9	0.681
P134	PSZ1G134.59+53.41	11 51 21.62	62 21 00.18	106.5 × 164.3	80.0	0.590	20.1 × 25.7	−86.2	0.592
P138	PSZ1G138.11+42.03	10 27 59.07	70 35 19.51	51.1 × 246.7	68.2	2.170	20.6 × 26.1	75.0	0.982
<b>P170</b>	PSZ1G171.01+39.44	08 51 05.10	48 30 18.14	119.0 × 126.8	−18.3	0.422	16.7 × 24.5	68.2	0.469
<b>P187</b>	PSZ1G187.53+21.92	07 32 18.01	31 38 39.03	104.0 × 145.3	−60.9	0.411	16.7 × 23.7	63.0	0.412
<b>P190</b>	PSZ1G190.68+66.46	11 06 04.09	33 33 45.23	109.0 × 180.1	−48.7	0.450	17.1 × 26.3	−86.6	0.356
<b>P205</b>	PSZ1G205.85+73.77	11 38 13.47	27 55 05.62	117.8 × 130.1	−35.9	0.385	16.9 × 23.9	65.2	0.431
P264	–	10 44 48.19	−17 31 53.90	102.9 × 124.9	−12.3	0.476	16.8 × 24.8	7.1	0.513
<b>P351</b>	–	15 04 04.90	−6 07 15.25	96.5 × 109.6	−39.9	0.355	17.2 × 19.7	11.6	0.392

<sup>a</sup>Since the cluster selection criteria, as well as the data for the cluster extraction, are different to those for the PSZ catalogue, not all the clusters in this work have an official PLANCK ID.

<sup>b</sup>Synthesized beam FWHM (in arcsec) and position angle measured from N through E.

<sup>c</sup>Achieved rms noise in corresponding maps.

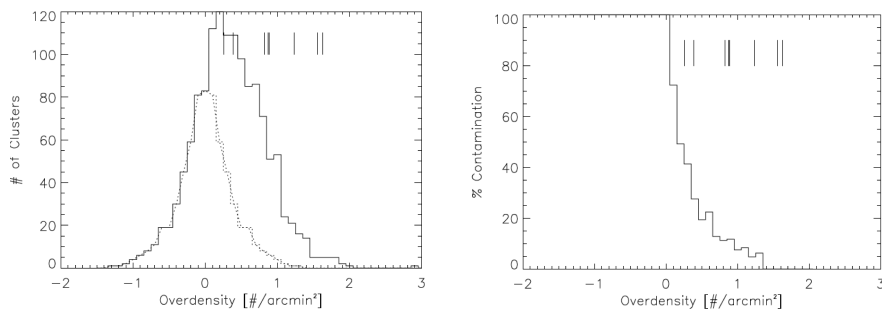


**Figure 1.** Left: the average *WISE*-object overdensities at the location of *Planck* cluster candidates, where overdensities were calculated as the average density of sources within a radius of 4.75 arcmin minus the average density of sources in an annulus with inner and outer radii of 4.75 and 7 arcmin. Here, *Planck* clusters are all 1362 identified SZ-cluster candidates in the all-sky maps; this will include known clusters as well as candidate clusters discovered by *Planck* that are yet to be confirmed. The dotted line is the positive mirror image of the negative side of the histogram. The vertical lines in both plots show the typical overdensities for our CARMA-8-detected cluster candidates. Right: percentage of clusters at a particular overdensity that do not have statistically significant overdensities. The statistical significance is calculated as the ratio between the number of clusters at a particular overdensity and the number of clusters expected if the overdensity distribution followed a Gaussian centred on 0. Thus, at an overdensity of 0.75 galaxies arcmin<sup>-2</sup>, the percentage contamination is <15 per cent – the ratio between the dotted curve and the solid histogram in the left-hand panel – and at overdensities of ≈1.25 galaxies arcmin<sup>-2</sup> (a typical *WISE* overdensity value for our *WISE*-*Planck* clusters) the contamination is <5 per cent.

cut for our sample selection is to exclude contaminating foreground sources, while that of the distance cut is to maximize the likelihood of the red object being associated with the *WISE* overdensity (and, hence, the *Planck* candidate cluster).

We note that there is some scatter in the mid-infrared (MIR) colour relation and some spread in the range of possible evolutionary tracks. Such that, in principle, lower redshift objects mimicking the  $z > 1$  *WISE* colours could lie within our sample. Though we do not expect to have targeted many  $z < 0.5$  objects as it is likely that they would have been detected by other instruments and surveys,

and a large fraction of our cluster candidates do not lie in close proximity to a confirmed cluster of sufficient mass (see Table C1). Our goal is to eventually use spectroscopic data to obtain accurate redshift estimates. Objects are considered red if their flux in *WISE* channel 1 (3.4 microns) minus channel 2 (4.6 microns)  $> -0.1$  in AB mag (0.5 in Vega); a method for preferentially identifying  $z > 1$  objects (Papovich 2008). This MIR colour criterion has been used by e.g. Galametz et al. (2012) and Brodwin et al. (2012), who have also followed-up galaxy overdensities at  $z = 1.75$  with CARMA-8.

Upon identifying *WISE* galaxy overdensities at *Planck* candidate-cluster locations, we discarded systems with high interstellar medium (ISM) contamination, as measured in the *IRAS* 100  $\mu\text{m}$  intensity band, as they are more likely to be spurious detections, and those at  $\delta < -10^\circ$  in order to ensure sufficient  $uv$ -coverage of the CARMA-8 data. We assigned a figure of merit to the remaining cluster candidates based on several parameters: distance of the *WISE* brightest red object within 2.5 arcmin from the *Planck* candidate-cluster position, the signal-to-noise ratio (SNR) in *Planck*, and the magnitude of the *WISE* overdensity, and drew our final sample from the highest priority objects.

### 3 CARMA-8 OBSERVATIONS

#### 3.1 Data processing

CARMA-8 observations were obtained towards 19 *Planck*-selected cluster candidates. Initially, data were collected for each cluster candidate for  $\approx 4$  h; if a clear or tentative SZ decrement appeared in the maps, more data were gathered on that object to improve the SNR of the detection; otherwise, no more observations were queued for that particular system. This was an observing strategy designed to maximize the number of detections in the limited CARMA-8 time at our disposal ( $\approx 110$  h) and, as a result, there is significant spread in the rms of our final visibilities. The noise levels are provided in Table 1, together with pointing centres, shorthand cluster IDs – which will be used throughout this work – and information on the beam, which is a measure of resolution.

Each cluster observation was interleaved every 15 min with data towards a bright, unresolved source to correct for variations in the instrumental gain. Absolute calibration was undertaken with observations of Mars. The raw data were exported in *MIRIAD* form and converted into a *MATLAB* format in order to be processed by the CARMA in-house data reduction software, which removes bad data points (e.g. visibilities that are shadowed, obtained during periods of sharp rises in system temperature or when the instrumental response changes unexpectedly or without calibrator data) and corrects for instrumental phase and amplitude variations; for further details see Muchovej et al. (2007). The output *uvfits* file from the pipeline contains calibrated visibilities ( $V$ ) – the response of the interferometer for a single baseline or the Fourier transform of the sky brightness distribution times the PB – which, for small fields of view (FoVs) like that of the CARMA-8 pointed observations, can be approximated by

$$V(u, v) = \iint A_N(l, m) I(l, m) \times \exp(-2\pi j[ul + vm]) dl dm, \quad (1)$$

where  $A_N$  is the normalized antenna beam pattern,  $I(l, m)$  is the sky intensity distribution,  $u$  and  $v$  are the baseline lengths projected on to the plane of the sky, and  $l$  and  $m$  are the direction cosines measured with respect to the  $(u, v)$  axes. The interferometer only measures some visibility values in the  $uv$ -plane. Hence, the array returns a sampled visibility function  $S(u, v)V(u, v)$ , where  $S(u, v)$  is a function known as the *synthesized beam* that equals one for sampled visibilities and zero otherwise. By applying an inverse Fourier transform to the sampled visibilities measured by the array, the sky image (or *dirty map*) can be recovered. In order to reconstruct the sky brightness distribution from an incomplete visibility map, we use a deconvolution algorithm: *CLEAN* (Högbom 1974).

#### 3.2 Radio-source contamination

In order to remove contaminating radio sources from the SB data, the LB CARMA-8 data were used to identify the location of the compact radio sources and provide an initial estimate of their peak flux density. This initial set of source parameters was fit directly to the LB visibility data and the best-fitting parameters were determined using the *DIFMAP* task *MODELFIT* (Shepherd 1997). Using these best-fitting parameters, the contribution to the SB data from detected LB radio sources was removed. Radio-source-subtracted, *CLEANED*<sup>7</sup> maps were produced, see Fig. 2 for CARMA-8 SZ-detected clusters, and Fig. A1 for candidate clusters without a CARMA-8 detection. Details on the SZ signal detected by CARMA and *Planck* are given in Table 2. For those CARMA-8 data that required the contribution from LB-detected radio sources to be removed, the reader should note that the source-subtracted SB images represent the map with the most likely source parameters and, thus, uncertainties in the source parameters are not reflected in the final map. Given that the cluster and source parameters can be degenerate, a quantitative analysis should fit for the cluster and radio-source contributions jointly. This analysis is undertaken in Paper II of this work (Rodríguez-González et al. in preparation).

Compact radio sources were detected in the LB CARMA-8 towards 12 cluster candidates; information on their properties is provided in Table 3. The LB-inferred radio-source environment towards candidate clusters with a CARMA-8 detection is, for the most part, benign, such that it has little or no effect on the SZ signal in the source-subtracted SB data. We find that this is not the case for a large fraction of the candidate clusters without a CARMA-8 detection, particularly for P031, P049, P052, P057, P121 and P138.

Noise levels in our LB data (on average  $\approx 520 \mu\text{Jy beam}^{-1}$ ) are comparable to typical noise levels in the NRAO VLA Sky Survey (NVSS) ( $\approx 500$ – $1000 \mu\text{Jy beam}^{-1}$ ) but, since radio sources tend to be brighter at lower frequencies, NVSS often provides a more complete image of radio-emitting sources. Hence, we predict the 31 GHz radio-source environment by extrapolating NVSS ('fitted') peak flux densities for radio sources located within 10 arcmin of our map centre assuming a value for the spectral index,  $\alpha$ . Our choice of  $\alpha$  is based on the average 1.4-to-31 GHz spectral index derived from matching sources in NVSS and our LB CARMA-8 data (Table 3). In Table 4 we present the position of those NVSS sources that, given our assumptions, we would expect to find at a significance of  $4\sigma$  or greater in the LB CARMA-8 data but, instead, remained undetected. A total of four radio sources satisfy these criteria. All but one of these sources (in the FoV of P109) are at  $\gtrsim 6$  arcmin from the map centre, with a predicted, attenuated 31 GHz peak flux density of  $< 3.5$  mJy and, hence, should have a negligible impact on the recovered SZ signal. Undetected sources in P109 have the potential to have the most impact on the recovered SZ signal, with a source expected to have an attenuated 31 GHz peak flux density of 4.0 mJy an arcminute away from the map centre. However, some of these sources could be varying, or could have flatter or inverted spectra, implying they could be brighter at 31 GHz than our predictions in Table 3. To estimate the contribution from radio sources below our detection threshold ( $4\sigma \approx 1.5 \text{ mJy beam}^{-1}$ ), we use a study by Murphy et al. (in preparation), which stacks 30 GHz *Planck* data at the position of NVSS-detected radio sources of similar flux density. We expect to suffer from  $\approx 90 \mu\text{Jy beam}^{-1}$  of contamination from confused radio sources, which would account for 2–6 per cent of the peak SZ decrement of our clusters (Table 2).

<sup>7</sup> *CLEANING* was undertaken with a tight box around the cluster signal, where present, otherwise no box was used.

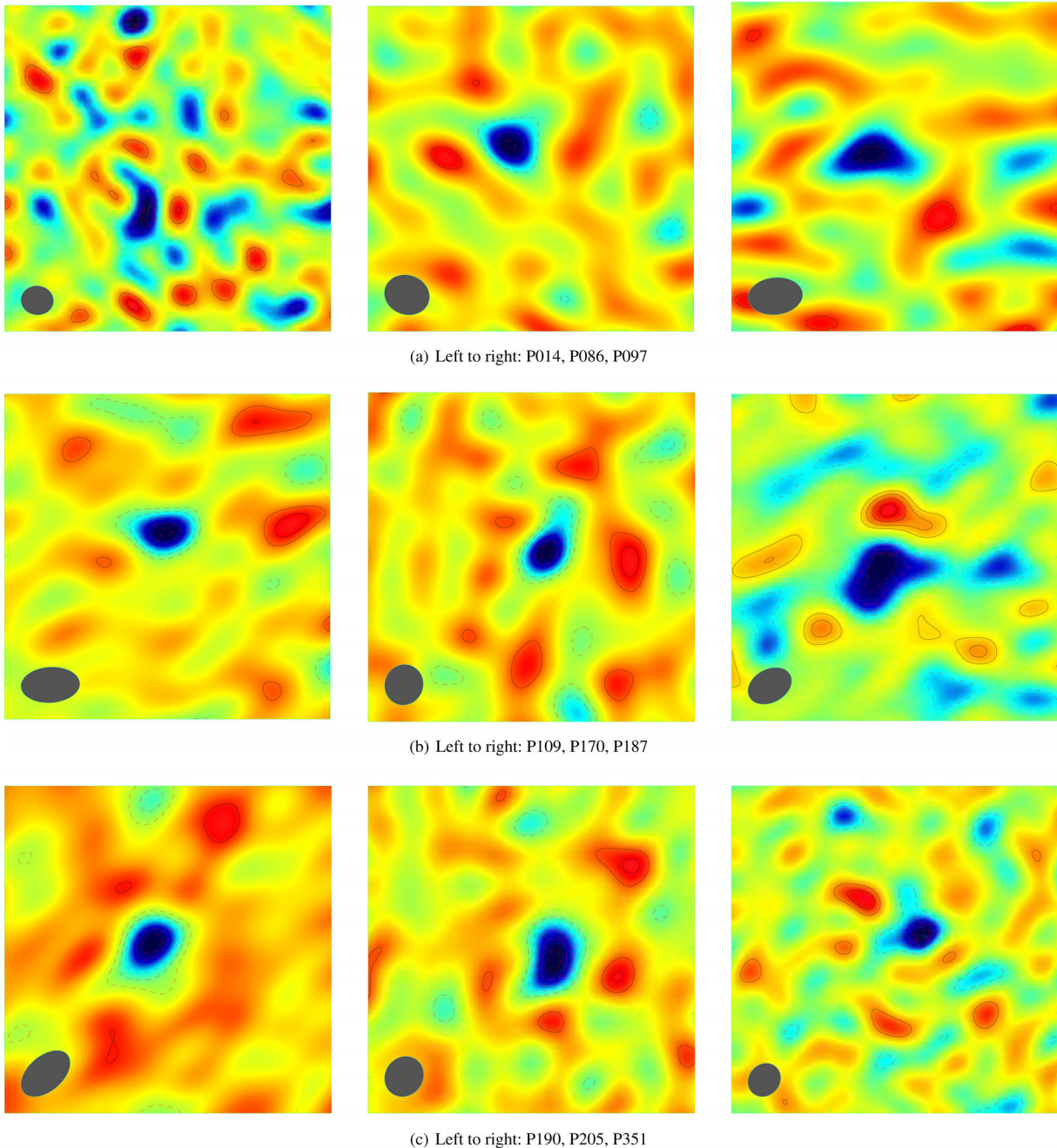


**Figure 2.** CLEANED, naturally weighted maps of the SB data for CARMA-detected clusters after radio-source subtraction, where necessary. The dimensions are  $1000 \text{ arcsec} \times 1000 \text{ arcsec}$  centred at the pointing centre. This is about twice the *Planck* beam FWHM (7–10 arcmin) relevant for SZ detection. Contours are scaled linearly starting from 2 to  $10\sigma$ , where  $\sigma$  is the noise on the map (Table 1), in integer multiples. Positive contours are shown in solid, black lines while negative contours are shown in dashed, red lines. The grey ellipse in the bottom-left corner of each map is the synthesized beam. No PB correction has been applied. Table 2 contains the value for the measured peak SZ flux density and information on detected radio sources is provided in Table 3.

### 3.3 CARMA SZ detections

8 of the targeted 19 cluster candidates were detected with a peak beam-corrected SZ-flux-density with an  $\text{SNR} \geq 4.4$  (Table 2).<sup>8</sup> We also found one tentative detection with an SNR of 4.2, which we deem tentative due to uncertainties in the data (see Appendix B).

<sup>8</sup> The SNR for the CARMA SZ detections was calculated as the ratio of the peak decrement, after correcting for beam attenuation, and the rms of the SB data.

Clusters have been classified as detections based on the inspection of the SB and LB CARMA-8 maps, taking into consideration ancillary data, which will be presented in detail in Section 4.1. For each cluster candidate we describe in Appendix B the CARMA-8 data, including the SZ signal and the radio-source environment.

The PB-corrected peak flux density of the SZ decrements in the CARMA-8 data (after source subtraction, where necessary) ranges between  $-1.5$  and  $-4.2 \text{ mJy beam}^{-1}$ , where P014 – a marginal detection – has the smallest decrement. The SNR of the SZ signals in the CARMA data ranges between 4.4 (for P097) and 7.8 (P190).

**Table 2.** Cluster-candidate information. For the peak of the SZ decrement in the CARMA-8 SB CLEANED, radio-source-subtracted maps, we provide the RA and Dec. coordinates, the peak flux density after correcting for PB attenuation and the distance to the map centre (coincident with the *Planck* position). Using the PB-corrected peak SZ flux density<sup>a</sup> and the rms of the SB data, we calculate the SNR of the CARMA-8 detection. Also included are the SNRs in our analysis of *Planck* data and, where available, from the *Planck* Union catalogue. The final column contains the *IRAS* estimate for the 100  $\mu$ m intensity within 5 arcmin of the pointing centre for our observations. Not all candidate clusters in our sample have positions in the Union catalogue, hence, for homogeneity, we centre the 100  $\mu$ m statistics on the CARMA-8 pointing centre. However, the typical offsets between the *Planck* Union catalogue positions and our CARMA-8 pointing centres, do not result in a significant change in the 100  $\mu$ m emission. This 100  $\mu$ m emission information can be retrieved from <http://irsa.ipac.caltech.edu/applications/DUST/>. Clusters that have been detected in the CARMA-8 data, even if marginally so, have their cluster ID written in bold font.

Cluster ID	RA ( <sup>h</sup> <sup>m</sup> <sup>s</sup> )	Dec. ( <sup>°</sup> <sup>'</sup> <sup>''</sup> )	PB-corrected peak SZ flux density (mJy beam <sup>-1</sup> )	Distance from map center (arcsec)	SNR CARMA-8	SNR <i>Planck</i>	SNR UNION	100 $\mu$ m emission (MJy sr <sup>-1</sup> )
<b>P014</b>	16 03 26.16	+03 16 48.00	-1.5	159	4.2	5.4	4.5	5.32 ± 0.35
P028	–	–	–	–	–	5.2	5.1	1.54 ± 0.01
P031	–	–	–	–	–	4.1	–	3.26 ± 0.06
P049	–	–	–	–	–	4.3	–	0.67 ± 0.04
P052	–	–	–	–	–	5.1	–	4.27 ± 0.15
P057	–	–	–	–	–	5.3	4.6	0.99 ± 0.03
<b>P086</b>	15 14 00.42	+52 47 49.55	-3.4	94	5.1	5.1	4.6	0.77 ± 0.02
P090	–	–	–	–	–	5.5	5.4	0.59 ± 0.02
<b>P097</b>	14 55 23.79	+58 52 18.42	-3.0	84	4.4	4.8	–	0.58 ± 0.03
<b>P109</b>	18 23 08.14	+78 23 04.18	-4.2	76	7.3	5.6	5.3	2.63 ± 0.06
P121	–	–	–	–	–	5.0	5.6	0.93 ± 0.11
P134	–	–	–	–	–	4.6	5.0	0.91 ± 0.06
P138	–	–	–	–	–	4.6	5.1	2.03 ± 0.04
<b>P170</b>	08 51 00.67	+48 30 30.13	-3.1	45	7.3	5.8	6.7	1.32 ± 0.03
<b>P187</b>	07 32 21.15	+31 38 11.02	-2.4	49	5.8	6.0	6.1	2.55 ± 0.08
<b>P190</b>	11 06 08.09	+33 34 00.22	-3.6	52	7.8	4.1	4.6	1.06 ± 0.05
<b>P205</b>	11 38 07.82	+27 54 30.61	-2.6	83	5.7	5.9	5.7	1.10 ± 0.01
P264	–	–	–	–	–	4.2	–	1.61 ± 0.02
<b>P351</b>	15 03 59.21	-06 06 30.25	-2.1	96	5.6	3.8	–	3.60 ± 0.04

<sup>a</sup>To correct the measured peak flux density for the effects of PB attenuation, we divide it by  $\exp^{-r^2/(2 \times \sigma^2)}$ , where  $r$  is the distance from the map centre to the pixel with the peak flux density of the radio source and  $\sigma = \text{Beam FWHM}/(2 \times (2 \times \log_e(2))^{0.5})$ .

The peak of the CARMA-8 SZ signals is within 2 arcmin of the *Planck* position for all systems but for P014, which is  $\approx 2.7$  arcmin away (see Table 2).

### 3.4 Potential reasons for CARMA-8 non-detections of the remaining candidate clusters

The data towards 10 cluster candidates did not show a significant decrement; though this does not provide conclusive evidence, in all cases, that the *Planck* cluster candidate is a spurious detection. A combination of factors could be responsible for the lack of an SZ signal in the CARMA-8 data (see Section 5.1 for comments on each of the undetected targets). These factors include, high noise levels in the SB data, confused radio sources (most relevant for observations with high rms in the LB data), poor subtraction of LB-detected radio sources and the cluster being significantly offset from the map centre, which results in strong beam attenuation. For example, a cluster with a relatively low peak-flux density of  $-1.5$  mJy beam<sup>-1</sup>, at 3 arcmin (at 4 arcmin) from the map centre would have a flux density on the CARMA SB map of  $-1.2$  mJy beam<sup>-1</sup> ( $-1.0$  mJy beam<sup>-1</sup>). Given that the typical range of rms values in the CARMA-8 SB data range between  $\approx 400$  and  $600$   $\mu$ Jy beam<sup>-1</sup>, such a signal would have, at best, an SNR  $\approx 2-3$  (1.7–2.6) and, hence, would not be registered as a solid detection. This highlights one of the challenges of high-resolution interferometric follow-up of clusters detected by a large beam experiment such as *Planck*. Radio sources are often the dominant contaminant to the CARMA-8 observations. If they are not subtracted properly or they are not detected above the background

noise – and, therefore, are not accounted for – they can fill and/or distort the SZ decrement.

## 4 VALIDATION

We discuss the reliability of the cluster candidates in our sample by (1) searching for evidence for the presence of a cluster in catalogues in the literature and as excess emission in the *ROSAT* X-ray data and (2) by considering the effects of ISM contamination to the *Planck* data.

### 4.1 Confirming the presence of a cluster in the CARMA-8 data through ancillary data sets

*Cluster catalogues in the literature.* In Table C1 we provide details on known clusters found in the SIMBAD data base (Wenger et al. 2000) and in the Wen, Han & Liu (2012) SDSS-based catalogue within 4 arcmin of the map centre of our observations. At least one such match was found for 13 of our clusters candidates. The CARMA-8 SZ signal for four of the systems in our sample – P170, P187, P190 and P205 – coincides with the location of a registered overdensity of galaxies from Wen et al., with redshift estimates ranging from  $\approx 0.2$  to  $0.5$ ; though only P187 has spectroscopic confirmation.

Seven of our cluster candidates without a CARMA-8 SZ signal were found to have a known cluster (or cluster candidate) within 4 arcmin of the map centre. In most cases, the lack of a CARMA-8 SZ signal towards these systems can be attributed to a

**Table 3.** Information on the radio-source environment towards our candidate clusters obtained from the LB CARMA-8 data and NVSS. Column 1 contains the ID name for the cluster candidate in whose FoV the radio source lies in. Columns 2 and 3 contain the RA and Dec. of the pixel with the peak flux density of the point source. At this position, and with this peak flux density as a starting point, the `DIFMAP` task `MODELFIT` was used to obtain a best-fitting peak flux density by chi-squared minimization. This best-fitting value, after PB correction, is given in the 5th column. The distance from the radio source to the map centre is provided in column 4. In column 6 we report, where available, the 1.4 GHz NVSS (fitted) peak flux density for the LB-identified radio source. The ‘fitted’ flux density values in NVSS refer to the peak surface brightness. We note that, unless stated otherwise, we will henceforth refer to flux density as the PB-corrected flux density. From the LB and NVSS peak flux densities, we calculate a spectral index between 1.4 and 31 GHz,  $\alpha$ , where  $S_\nu \propto \nu^{-\alpha}$ , with  $S$  denoting flux and  $\nu$  frequency. It should be noted that the NVSS and CARMA data were taken years apart and variability could affect  $\alpha$ . The mean value for  $\alpha$  is 0.72. Clusters that have been detected in the CARMA-8 data, even if marginally so, have their cluster ID written in bold font.

Cluster ID	RA ( <sup>h</sup> <sup>m</sup> <sup>s</sup> )	Dec. ( <sup>°</sup> <sup>'</sup> <sup>''</sup> )	Distance from map centre (arcsec)	31 GHz peak flux density (mJy)	1.4 GHz peak flux density (mJy)	$\alpha$ (1.4/31 GHz)
<b>P014</b>	16 03 18.90	+03 16 44.00	152	6.3	120.8	0.95
<b>P014</b>	16 03 30.20	+03 26 32.00	458	9.4	96.8	0.75
P028	15 40 13.24	+17 56 33.14	134	3.7	21.9	0.57
P028	15 40 21.92	+17 52 45.12	196	3.2	77.7	1.02
P031	15 27 30.42	+20 41 32.27	113	3.4	–	–
P049	14 44 27.84	+31 13 15.87	133	10.0	62.6	0.59
P052	21 18 49.08	+00 33 28.00	202	5.6	129.4	1.01
P052	21 19 05.08	+00 32 40.00	44	2.5	56.3	1.00
P057	15 48 49.32	+36 10 29.80	240	3.4	68.6	0.97
P057	15 48 41.06	+36 09 33.85	130	3.2	7.6	0.28
<b>P109</b>	18 22 52.25	+78 23 04.18	76	2.6	–	–
P121	13 02 40.94	+67 28 42.30	311	23.2	317.1	0.84
P138	10 26 37.40	+70 32 50.37	432	150.3	135.1	–0.03
<b>P170</b>	08 51 14.78	+48 37 06.11	421	10.8	119.9	0.78
<b>P187</b>	07 32 20.21	+31 41 19.03	161	3.1	12.7	0.46
<b>P351</b>	15 04 18.65	–06 05 15.24	237	3.3	51.7	0.89

**Table 4.** Predicted 31 GHz flux densities after PB attenuation for radio sources detected in NVSS within 10 arcmin of our map centre but without a counterpart in the LB CARMA-8 data. These flux densities were calculated using the mean 1.4–31 GHz spectral index (0.72) derived from radio sources detected in NVSS and our CARMA-8 data. We present only those sources whose estimated (attenuated) 31 GHz flux density is at least four times the noise in the LB CARMA-8 data. The expected SNR in the LB CARMA-8 data is provided in the last column. This was calculated using the LB rms and the expected 31 GHz beam-attenuated peak flux density.

Cluster ID	RA ( <sup>h</sup> <sup>m</sup> <sup>s</sup> )	Dec. ( <sup>°</sup> <sup>'</sup> <sup>''</sup> )	Distance (arcsec)	Predicted, PB-attenuated 31 GHz peak flux density (mJy)	SNR
P052	21 18 48.31	0 37 46.3	356	2.4	6.1
P052	21 19 25.44	0 31 42.1	354	3.3	8.6
P109	18 22 40.96	78 22 20.2	64.6	4.0	7.7
P190	11 05 53.78	33 40 53.3	447	2.4	6.9

combination of one or more of the following: challenging radio-source environment, high rms of the SB visibility data, PB attenuation and insufficient ICM cluster mass (deduced from the X-ray data or estimated from the richness value). For further details on each CARMA-detected system see Appendix B, and Section 5.1 for the remaining systems.

*ROSAT X-ray data.* *ROSAT* X-ray images for each of our cluster candidates without (and with) a CARMA-8 SZ detection are provided in Appendix A (and Appendix E). For the eight candidate clusters with a clear CARMA-8 detection, there is compelling evidence for X-ray cluster emission within a few arcminutes towards all of them, though the peak of the X-ray emission lies outside the

CARMA SZ contours for two systems, P109 and P170. For P014 – the candidate cluster with the tentative CARMA detection – there is no support for the presence of a cluster from the *ROSAT* image. Regarding the cluster candidates without a CARMA SZ detection, three seem to have evidence for extended X-ray emission in the *ROSAT* data: P049, P090 and P138.

#### 4.2 Investigating 100 $\mu\text{m}$ ISM contamination in the *Planck* data

*Planck* uses a multifrequency matched filter to detect both the SZ increment and the SZ decrement from a cluster. Due to strong ISM

contamination in the upper frequencies (353, 545, 857 GHz), the SZ increment may be biased high, resulting in a spurious detection, especially if the ISM emission falls on top of a CMB cold spot. In Table 2 the 100  $\mu\text{m}$  emission within 5 arcmin from the pointing centres of the CARMA-8 cluster observations is provided. The mean 100  $\mu\text{m}$  emission is  $1.68 \pm 0.02 \text{ MJy sr}^{-1}$  towards clusters without a CARMA-8 detection and  $2.10 \pm 0.01 \text{ MJy sr}^{-1}$  for those with a clear detection. Hence, the presence of this foreground does not correlate strongly with detectability, at least for cluster candidates in our sample. The candidate cluster suffering from the highest ISM contamination is P014 with  $5.3 \pm 0.4 \text{ MJy sr}^{-1}$ . This system also shows the largest positional offset between the *Planck* and CARMA-8 data but the ISM contamination is not sufficient, in this case, to account alone for such a large discrepancy.

## 5 DISCUSSION

### 5.1 Are any of the candidate clusters without a CARMA-8 detection likely to be real?

We investigate the likelihood of the candidate clusters without a CARMA-8 detection being *real* clusters by considering all the relevant data available to us. That is, we consider the ensemble of the CARMA-8 data (Table 1), the NVSS catalogue of radio sources (Table 4), the *Planck* data (Table 2), contamination in the *Planck* data from the 100  $\mu\text{m}$  emission (Table 2), ancillary data (Section 4.1) including the *ROSAT* images (Appendix A and E) and evidence in the literature for the presence of other clusters within 4 arcmin of the map centre of the CARMA images (Table C1). A summary of these results is given in Table 5.

**P028:** radio-source contamination in the CARMA-8 data is low. In the SB data there is a  $2\sigma$  negative feature  $<2$  arcmin away from the pointing centre but this is not an isolated  $2\sigma$  feature in the map. The SNR in *Planck* is quite high, 5.1, but could be affected by ISM emission ( $\approx 1.54 \text{ MJy sr}^{-1}$ ). No X-ray emission is seen in the *ROSAT* image. It seems unlikely that there is a single massive

cluster associated with P028. But, since there are three low-mass (candidate) clusters catalogued in the literature within 3 arcmin of the CARMA-8 observations, with  $0.07 \lesssim z \lesssim 0.4$ , it could be that *Planck* picks up a combined SZ signal due to its large beam size.

**P031:** has no decrement in the CARMA-8 data that could reliably be attributed to a low-SNR SZ signature, since the ones present in the map are likely to be a product of the inadequate subtraction of an extended radio source. The *Planck* data yields a low-SNR cluster signal and suffers from high ISM contribution. There is no cluster detection in the *ROSAT* image. Thus, we conclude that, most likely, this is a spurious *Planck* cluster candidate.

**P049:** the challenging radio-source environment could be responsible for the lack of a CARMA-8 detection towards P049. The SNR in *Planck* is moderate, but contamination from ISM emission is low, which reduces uncertainties in the SNR value. The *ROSAT* image shows extended X-ray emission, with three point sources – a strong indication that there is a cluster towards P049.

**P052:** a  $3\sigma$  ( $\approx -1.2 \text{ mJy beam}^{-1}$ ) feature is detected in the radio-source-subtracted SB data within 2 arcmin of the pointing centre. The high level of radio-source contamination could be filling in partly an SZ decrement. This system appears in the *Planck* data with an SNR of 5.1, but these data suffer from high ISM emission. No X-ray cluster emission is seen in the *ROSAT* data. Overall, P052 does not seem a robust cluster candidate.

**P057:** radio-source contamination in the CARMA data is substantial. The SNR in *Planck* is moderate and no cluster signal is seen in the *ROSAT* image.

**P090:** there is a clear cluster detection in the *ROSAT* data. The X-ray counts in these data are higher over a similar area than for another cluster P187 (Abell 586), which has an estimated mass within  $r_{200}$  – the radius at which the mean gas density is 200 times the critical density – of  $\gtrsim 5 h_{100}^{-1} M_{\odot}$  (AMI Consortium 2012), according to SZ measurements by the Arcminute Microkelvin Imager (Zwart et al. 2008). P090 has an SNR of 5.6 in the *Planck* data, which have negligible ISM contamination. Given all of this, it is surprising that, despite the seemingly benign radio-source environment and the low

**Table 5.** Qualitative summary of the information drawn from the main relevant data available towards those cluster candidates in our sample without a CARMA-8 SZ detection. Two tick marks indicate a strong presence of the emission of interest, while a single tick mark indicates a smaller contribution. Those systems for which the emission of interest is considered negligible are labelled with a cross mark. The SNRs given in the fourth column correspond to the most significant negative feature within  $\approx 3$  arcmin of the map centre. Those entries labelled with (I) do not appear in the Union catalogue and the SNRs come from an intermediate *Planck* data product. Based on this information, we include a comment on our own judgement on the likelihood of there being a real cluster in the neighbourhood of the CARMA map centre.

Cluster ID	Radio contamination	CARMA-8	<i>Planck</i>		<i>ROSAT</i>	Real?
		SB data	SNR	ISM <sup>a</sup>		
P028	✗	$2\sigma$ ( $\lesssim -0.9 \text{ mJy beam}^{-1}$ ) <sup>b</sup>	5.1	✓	✗	Unlikely
P031	✓	$3\sigma$ ( $\gtrsim -0.9 \text{ mJy beam}^{-1}$ ) <sup>c</sup>	4.1 (I)	✓✓	✗	Unlikely
P049	✓✓	$<2\sigma$ ( $\gtrsim -1 \text{ mJy beam}^{-1}$ )	4.3 (I)	✗	✓	Likely
P052	✓	$2\sigma$ ( $\lesssim -0.7 \text{ mJy beam}^{-1}$ )	5.1 (I)	✓✓	✗	Unlikely
P057	✓✓	$<2\sigma$ ( $\gtrsim -1 \text{ mJy beam}^{-1}$ )	4.6	✗	✗	Unknown
P090	✗	$2\sigma$ ( $\lesssim -0.8 \text{ mJy beam}^{-1}$ )	5.4	✗	✓	Likely
P121	✓✓	$<2\sigma$ ( $\gtrsim -1.6 \text{ mJy beam}^{-1}$ )	5.6	✗	✗	Unknown
P134	✗	$2\sigma$ ( $\lesssim -0.7 \text{ mJy beam}^{-1}$ )	5.0	✗	✗	Unknown
P138	✓✓	NA <sup>d</sup>	5.1	✓	✓	Likely
P264	✗	$2\sigma$ ( $\lesssim -1 \text{ mJy beam}^{-1}$ ) <sup>c</sup>	4.2 (I)	✓	✗	Unlikely

<sup>a</sup>One (two) tick marks refer to 100 micron emission greater than 1 MJy/sr (3 MJy/sr).

<sup>b</sup>The map contains several other negative features of similar SNR.

<sup>c</sup>The negative features coincide with features from interference or sidelobe patterns.

<sup>d</sup>This information is not meaningful for P138 given the poor  $uv$  coverage and high rms of the CARMA-8 SB data towards this system.

rms in the SB data, there is no clear SZ detection in the CARMA-8 data.

*P121*: has a moderate SNR in the *Planck* Union catalogue with low contamination from ISM emission. The CARMA-8 data are strongly affected by radio-source foregrounds and there is no sign of cluster-like X-ray emission in the *ROSAT* data.

*P134*: has a *Planck* SNR of 5.0, which should not be greatly affected by ISM emission. There is no indication of the presence of a cluster in the *ROSAT* data. Regarding the CARMA results, radio contamination is negligible and, while the rms is high,  $\approx 600 \mu\text{Jy beam}^{-1}$ , we would expect to detect a massive ( $\gtrsim -2.0 \text{ mJy beam}^{-1}$ ) cluster at  $\gtrsim 3\sigma$  and yet not even a  $2\sigma$  negative feature is seen within 3 arcmin of the map centre.

*P138*: has an SNR of 5.1 in the *Planck* Union catalogue, with little impact from ISM emission. This, together with the detection of extended X-ray emission in *ROSAT*, deem *P138* a robust cluster candidate. The lack of a CARMA-8 detection is not surprising given the complications with radio-source foreground removal and the exceedingly high rms and poor *uv* coverage due to the limited amount of data available towards this system.

*P264*: is most likely a spurious cluster candidate. The *Planck* data suffer from significant ISM contamination and yield a low SNR for *P264*. The *ROSAT* image shows no evidence of a cluster nor do the CARMA-8 data, despite the reasonable rms and benign radio-source environment.

## 6 REDSHIFT ESTIMATION

The higher resolution CARMA-8 data showed that the putative brightest cluster galaxy (BCG), on whose photometric redshift we relied on to select our  $z \gtrsim 1$  cluster candidates, did not lie within the CARMA-8 SZ contours for all but three of the systems: *P097*, *P109* and *P190*, see Appendix D. We now explore their plausible redshifts derived from photometric criterion. This is an independent approach, parallel to the XMM follow-up of *Planck* clusters, which

has yielded redshifts of many *Planck*-selected clusters (Planck Collaboration 2013c). We note that this analysis would be challenging to undertake without the CARMA-8 data since the location of the cluster would not be precisely known and, thereby, the galaxy counterparts might be difficult to identify.

### 6.1 The WISE colour criterion

In Fig. F1 (and F2) we explore the colour–magnitude distribution of *WISE* sources towards candidate clusters with (without) a CARMA detection within 2 arcmin of the CARMA (*Planck*) centroid. There does not appear to be any apparent difference in the number of red *WISE* galaxies for the CARMA-detected and -undetected clusters (Table 9). We overlay the tracks for a passively evolving starburst of mass  $10^{12} M_{\odot}$ , and an e-folding time-scale of star formation of 100 Myr using three formation redshifts for the burst. *WISE* objects satisfying the MIR colour criterion are shown as solid diamonds. The position of the brightest red object fainter than 15.8 mag at  $3.4 \mu\text{m}$  is circled. The colours of this red object had suggested that *P014*, *P170*, *P187*, *P190* and *P205* would be at  $z > 1$  using the  $[3.4] - [4.6] > -0.1$  AB mag criterion. However, this object was found to lie outside the CARMA-8 SZ contours in all but three of the detected systems. With the CARMA-8 data in hand, we searched the *WISE* catalogue for the brightest red object within 2.5 arcmin of the CARMA-8 SZ centroid; however, that only served to add *P109* to the list of  $z > 1$  candidate clusters.

#### 6.1.1 Reliability of WISE colours to identify $z > 1$ clusters?

Selection of high-redshift ( $z \gtrsim 1$ ) objects based on *WISE* or *Spitzer* colours has been discussed extensively in e.g. Papovich (2008), Gettings et al. (2012), Muzzin et al. (2013) and Rettura et al. (2014). We explore further the reliability of the *WISE* MIR colour criterion in Fig. 3 by looking at the relation between redshift and overdensity

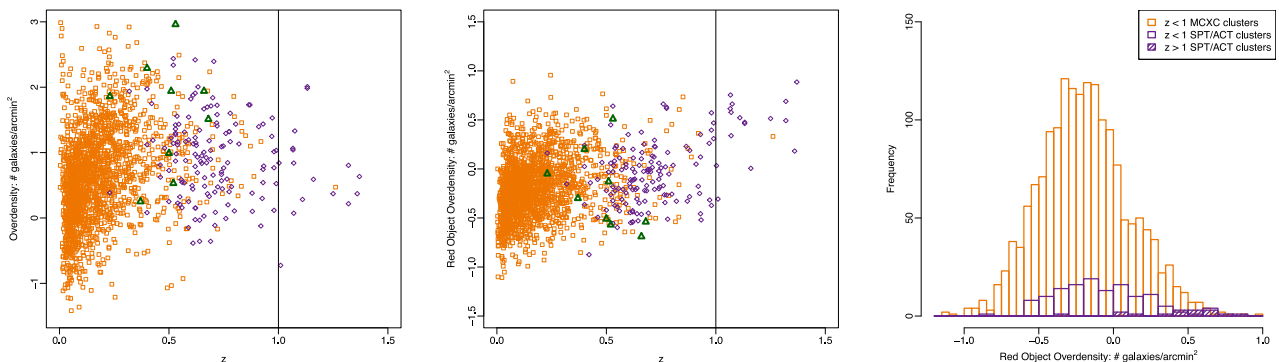


**Figure 3.** Left (and middle) panels: relation between redshift and the *WISE* all-object (red-object only) overdensity for (1) MCXC clusters (orange squares), (2) a selection of  $z > 0.5$  SPT and ACT-discovered clusters from Williamson et al. (2011), Marriage et al. (2011), Reichardt et al. (2013) and Hasselfield et al. (2013) (purple diamonds), whose redshifts can be spectroscopic or photometric and (3) *Planck* cluster candidates selected in this work with a CARMA-8 SZ detection (green triangles), where their redshifts are taken from Table 7. The overdensities have been calculated as the average density of *WISE* sources within a radius of 2 arcmin from the MCXC, SPT/ACT and CARMA centroids (as appropriate) minus the average density of sources in an annulus with inner and outer radii of 4.75 and 7 arcmin. The vertical lines are included to highlight where  $z = 1$ . These figures show that most of our cluster candidates are likely to be among the most massive known clusters at intermediate redshifts, which is not entirely surprising given that they were selected from *Planck* data, which are most sensitive to massive systems. The right-hand panel shows histograms for the red-object *WISE* overdensities within 2 arcmin for the MCXC clusters at  $z < 1$  (where only one cluster is at  $z > 1$ ) in orange and for the SPT/ACT clusters, where those at  $z < 1$  are shown in open bins with a purple border and those at  $z > 1$  are shown in bins filled with diagonal purple lines. We do not include the cluster candidates from this work as the numbers are small. While the overdensity of red objects is typically larger for clusters at  $z > 1$  than at lower redshifts, as one would expect from the application of the MIR criterion (e.g. Papovich 2008), the contamination is high, such that selection of  $z > 1$  clusters from red-object *WISE* overdensities alone might not be very reliable. The histograms for the  $z < 1$  clusters in the SPT/ACT and MCXC samples are skewed towards negative red-object overdensity values, but this is likely due to uncertainties in the calculation for the overdensity and background estimation, though further investigation is out of the scope of this work.

of *WISE* objects for a sample of clusters spanning a wide redshift range,  $0.02 < z < 1.4$ . We use two overdensity measurements – one which considers all *WISE* objects (left-hand panel) and another which only considers the red *WISE* objects, i.e. those that satisfy  $[3.4] - [4.6] > -0.1$  AB mag (middle panel). The orange squares represent the 345 X-ray-detected clusters from the MCXC catalogue (Piffaretti et al. 2011). Clusters discovered by SPT and ACT (Marriage et al. 2011; Williamson et al. 2011; Hasselfield et al. 2013; Reichardt et al. 2013) with  $z \gtrsim 0.5$  (where some of these redshifts are photometric), are displayed in purple diamonds. *Planck* cluster candidates selected in this study with a CARMA-8 detection are represented by green triangles. For our cluster candidates, we use the SDSS-derived redshifts from Table 7. The overdensities have been calculated as the average density of *WISE* sources within a radius of 2 arcmin from the MCXC, SPT/ACT and CARMA centroids (as appropriate) minus the average density of sources in an annulus with inner and outer radii of 4.75 and 7 arcmin. The mean *WISE*-all (and red-only) object overdensity for the MCXC clusters is 0.7 (−0.2) galaxies arcmin<sup>−2</sup>, with a standard deviation (s.d.) of 0.8 (0.3); for the CARMA-8 detections it is 1.6 (−0.23) galaxies arcmin<sup>−2</sup>, with a s.d. of 0.9 (0.4) and for the SPT/ACT clusters it is 0.9 (−0.1) galaxies arcmin<sup>−2</sup>, with a s.d. of 0.6 (0.3) for systems at  $z < 1$  and 0.73 (0.4), with a s.d. of 0.7 (0.3) for those at  $z > 1$ . Although we do not know if all the *WISE* objects are associated with the clusters, in a statistical sense, the average *WISE*-object overdensities for the different cluster sets suggests that our CARMA-8-detected clusters are likely to be massive systems. A strong correlation between *WISE* all object overdensity with redshift is not expected, though some selection effects could be manifesting themselves in the plot e.g. the highest redshift, X-ray-selected clusters are likely to be particularly massive, if they were serendipitous X-ray detections, and confusion in the *WISE* data is likely to have the highest impact at higher redshifts. The red-object criterion should be preferentially selecting  $z \gtrsim 1$  objects and, hence, we should expect a significant rise in the *WISE* red-object overdensity for systems at  $z > 1$ . While we do indeed see a rise in Fig. 3, middle panel, the histograms in the rightmost panel indicate that contamination levels are high. These contamination levels estimated from the positive inversion of the negative side of the red-object overdensity histograms for  $z < 1$  systems suggest that relying exclusively on red-object *WISE* overdensities for selecting  $z > 1$  clusters can be risky. We also find that there are some low-redshift ( $z \ll 1$ ) clusters that have large red-object overdensities. Again, this could be due to contamination. Otherwise, there may be an additional  $z > 1$  cluster within our 2 arcmin radius. There are also cases where  $z > 1$  background, unassociated objects could be producing an overdensity of red sources, in particular if a massive cluster is acting as gravitational lens, since such an effect would promote the detection of higher- $z$  galaxies located behind the cluster that would otherwise remain undetected. It is also known that the  $[3.4] - [4.6] > -0.1$  (AB mag) colour selection of  $z > 1$  objects can sometimes misidentify low-redshift systems. Possible scenarios where an object might be falsely identified as red include, when the presence of an AGN leads to a rise in the galaxy Spectral Energy Distribution (SED) at  $\approx 3.4 \mu\text{m}$  or when the  $3.3 \mu\text{m}$  polycyclic aromatic hydrocarbon emission line in star-forming galaxies at a range of  $z$  below 1 falls in the  $4.6\mu\text{m}$ -*WISE* band (see e.g. Stern et al. 2012; Assef et al. 2013 for methods on how to identify AGN in *WISE* data). A targeted spectroscopic campaign in these cluster fields will be able to distinguish between these possibilities.

## 6.2 The SDSS criterion

### 6.2.1 Calibrating the SDSS photometric redshift using a subset of MCXC clusters

We investigated the validity of using SDSS photometric redshifts, henceforth  $z_{\text{phot}}$ , of galaxies in the vicinity of known clusters to estimate the cluster redshift. To do this, first we selected clusters in the MCXC catalogue (Piffaretti et al. 2011) with  $M_{500} \geq 2.5 \times 10^{14} M_{\odot}$  and spectroscopic redshift  $z_{\text{spec}} \geq 0.5$ , in order to produce a cluster sample with similar properties to those expected for the *PLANCK*-discovered candidate clusters in this work. Secondly, we obtained  $z_{\text{phot}}$ s from SDSS for all the galaxies within 1.5 and 1 arcmin of the MCXC cluster centroid, where these radii were chosen for being representative of a typical cluster extent at  $z = 0.5$ . Histograms for the distribution of  $z_{\text{phot}}$ s within these two radii for each of the selected MCXC clusters are shown in Fig. G1.

We used two methods to estimate a value for the cluster  $z_{\text{phot}}$  and applied each method to the 1.5 and 1 arcmin results; the results for each method together with the spectroscopic cluster redshift are provided in Table 6. For the first method (‘all’), we took the mean of all the  $z_{\text{phot}}$  measurements; for the second method (‘histogram peak’), we took the mean of the  $z_{\text{phot}}$ s for objects lying in the histogram bin with the highest counts (Fig. G1). The difference between the cluster  $z_{\text{spec}}$  and the  $z_{\text{phot}}$  estimate for each of the methods is plotted in Fig. 4 as a function of  $z_{\text{phot}}$  for the MCXC clusters in Table 6. Uncertainties are not included in this plot for clarity but typical errors in the galaxy  $z_{\text{phot}}$ s in SDSS are  $\approx 0.1$ – $0.15$ .

From Fig. 4, it can be deduced that, regardless of the method employed, beyond  $z \approx 0.8$ , the photometric estimates do not provide a good match to the spectroscopic redshift, likely due to the poor sensitivity of SDSS in this redshift regime, although this is based on two data points only. This figure also shows that typically the SDSS  $z_{\text{phot}}$  estimates are larger than the spectroscopic values. Closer inspection of the  $z_{\text{phot}}$  distribution from Fig. G1 shows that, for the  $z \gtrsim 0.6$  systems, the histograms flatten out over a large portion of the redshift range. On other hand, until  $z \approx 0.6$  the (mean, absolute) differences between the photometric and spectroscopic redshifts is reasonably small,  $\lesssim 0.1$ , and the histograms tend to have narrow peaks (with typical widths of  $\approx 0.3$ ). The exception being RX J1728.6+7041. We find that the second method, when searching within a radius of 1.5 arcmin, provides the photometric redshifts closest to the spectroscopic value throughout most of the sampled redshift range; with the mean, absolute difference for the whole redshift range sampled being 0.08 and 0.06 for  $z < 0.6$ . However, as appealing as this result might be, the number of clusters in this study are scarce and thus it cannot provide conclusive evidence as to whether the sole use of SDSS photometric redshifts can be used in a widespread fashion to estimate redshifts for clusters in the intermediate-to-high- $z$  regime. More extensive efforts for cluster identification and redshift estimation using SDSS data are available in Rykoff et al. (2013) and have been applied to *Planck* cluster candidates in Rozo et al. (in preparation).

### 6.2.2 Application of the SDSS photometric redshifts to the CARMA-detected clusters candidates

Histograms for the distribution of SDSS galaxy  $z_{\text{phot}}$ s within 1 and 1.5 arcmin of the CARMA cluster centroids are given in Fig. G2. Comparing the number of SDSS objects found in the peak bin of

**Table 6.** Spectroscopic redshifts ( $z_{\text{spec}}$ ) for clusters in the MCXC catalogue (Piffaretti et al. 2011) with  $M_{500} \geq 2.5 \times 10^{14} M_{\text{sun}}$  and  $z \geq 0.5$  with SDSS coverage. Photometric redshifts from objects in the SDSS data base within 1.5 and 1 arcmin of the MCXC cluster position were used to estimate a photometric redshift for the cluster ( $z_{\text{phot}}$ ). We estimated  $z_{\text{phot}}$  in two ways: (1) using the mean photometric redshift for all objects within the radial search (ALL); (2) using the mean photometric redshift of objects within the radial search which fall within the peak bin of the histograms in Appendix G (histogram peak)<sup>a</sup>. The average uncertainty in  $z_{\text{phot}}$  in the SDSS data base for the relevant objects is typically between 0.1 and 0.15. Uncertainties are not included in the table since the mean SDSS  $z_{\text{phot}}$  error would be an underestimate. The last column contains photometric redshifts obtained from the analysis of Wen et al. (2012) of SDSS DR6 data, where available. The  $z_{\text{phot}}$ s in bold are the ones obtained from what was found to be the most reliable method.

MCXC Name	$z_{\text{spec}}$	$z_{\text{phot}}$ SDSS-DR9				$z_{\text{phot}}$ SDSS-DR6 (Wen et al. 2012)
		All (1.5 arcmin)	(1 arcmin)	Histogram peak (1.5 arcmin)	(1 arcmin)	
BVH 20072	0.50	0.42	0.40	<b>0.36</b>	0.52	NA
MACS J0911.2+1746	0.50	0.48	0.49	<b>0.52</b>	0.53	NA
BVH 2007198	0.52	0.41	0.42	<b>0.51</b>	0.51	0.4960
MACS J1423.8+2404	0.54	0.45	0.48	<b>0.51</b>	0.39	0.5197
MACS J0018.5+1626	0.55	0.47	0.47	<b>0.53</b>	0.52	0.5602
MACS J1149.5+2223	0.55	0.46	0.49	<b>0.53</b>	0.52	0.5603
MS 1241.5+1710	0.55	0.47	0.49	<b>0.39</b>	0.52	0.5572
RXC J1728.6+7041	0.55	0.44	0.37	<b>0.35</b>	0.35	NA
WARP J0942.3+8111	0.55	0.44	0.47	<b>0.54</b>	0.55	NA
BVH 2007123	0.56	0.49	0.52	<b>0.53</b>	0.53	0.5839
MACS J2129.4−0741	0.59	0.50	0.52	<b>0.54</b>	0.55	0.6324
BVH 2007122	0.60	0.50	0.53	<b>0.53</b>	0.68	0.6055
BVH 2007173	0.62	0.44	0.43	<b>0.66</b>	0.23	0.5470
BVH 2007149	0.70	0.55	0.58	<b>0.66</b>	0.65	NA
MACS J0744.9+3927	0.70	0.48	0.49	<b>0.68</b>	0.68	NA
WARP J1350.8+6007	0.80	0.47	0.54	<b>0.69</b>	0.70	NA
BVH 2007154	0.89	0.43	0.50	<b>0.46</b>	0.52	NA

<sup>a</sup>When calculating the photometric redshift estimate using method 2 (i.e. from the histogram peak) for histograms with multiple peaks, we took the mean value for all the objects in all those bins.

the histograms for our CARMA-detected clusters and the selected MCXC clusters, shows that the former are very likely to be very massive systems since mass is expected to be correlated with optical richness. For four clusters, P170, P187, P190 and P205, the histograms shows a distinctive narrow peak; for two clusters, P014 and P097, such a feature is not as prominent; and for P086 the distribution is bimodal while for P109 it is almost uniform out to  $z = 0.9$ . The mean  $z_{\text{phot}}$  estimates for the three methods outlined in the previous section are provided in Table 7. The mean  $z_{\text{phot}}$  for all CARMA-detected systems from our sample using method three with a radial search of 1.5 arcmin – the preferred method from results in Section 6.2.1 – is  $\approx 0.5$ ; results from this method are highlighted in Table 7.

We expect the histograms in Figs G1 and G2 to be biased towards low-redshift objects, since the sensitivity of SDSS drops as a function of redshift and the catalogue is not expected to be very complete at  $z \gtrsim 0.3$  (e.g. Montero-Dorta & Prada 2009). Hence, for clusters like P014 and P187 with the  $z_{\text{phot}}$  distribution leaning towards  $z \lesssim 0.4$ , it is hard to rule out completely the possibility of a chance superposition of a low- and a high-redshift cluster without deep spectroscopic data. Though the lack of significant peaks in the  $z_{\text{phot}}$  distribution at higher redshifts, – where ‘significance’ is measured in terms of total number of galaxies in the ‘peak’ bin and relative to the other bins – is a strong indication that it is the likely, approximate redshift of the cluster.

To investigate the possibility of a higher redshift cluster being associated with our cluster candidates, we found out how many of the SDSS objects towards each system had a matching *WISE* object within 3 arcsec (FWHM of the *WISE* short channels  $\approx 6$  arcsec). If

there was a high-redshift cluster that was not seen in the relatively shallow SDSS data, there should be an overdensity of *WISE* red objects without an SDSS counterpart<sup>9</sup> (see Table 8; note that for this overdensity calculation, unlike for earlier ones, no background galaxy contribution has been applied, since SDSS objects have been removed on the basis that they are likely to be low- $z$  interlopers). P170 has the largest overdensity of *WISE*, red, unmatched objects and P187 the lowest, which provides further evidence that this cluster is indeed Abell 586 at  $z \sim 0.2$ . It is surprising that P109, a cluster that displayed an unconstrained SDSS galaxy- $z_{\text{phot}}$  distribution compared to P187 (Fig. G2), has an overdensity of these objects as low as  $0.29 \text{ arcmin}^{-2}$ . One possibility is that the cluster is between  $0.6 \lesssim z \lesssim 1$ ; then it might not have many objects that satisfy the MIR colour criterion nor that are detected in SDSS. Alternately, most of the galaxies of this cluster may be below the *WISE* detection threshold, or confused by foreground sources within the large beams of the short-wavelength channels, which is more likely to happen in  $z \gg 1$  systems. Thus, based on our analysis of SDSS photometric redshifts, the *WISE* MIR colour criterion that we initially adopted appears to overestimate the redshifts of our detected clusters. However, spectroscopic observations of large numbers of galaxy members of the clusters, is required for a definitive confirmation of the redshift. NIR long-slit spectroscopy of one of the galaxies associated with the P097 SZ decrement is presented in Paper II (Rodríguez-González et al. in preparation) and appears to agree with the SDSS photometric redshift.

<sup>9</sup> *WISE* objects with two or more blended components or flagged as extended were removed.

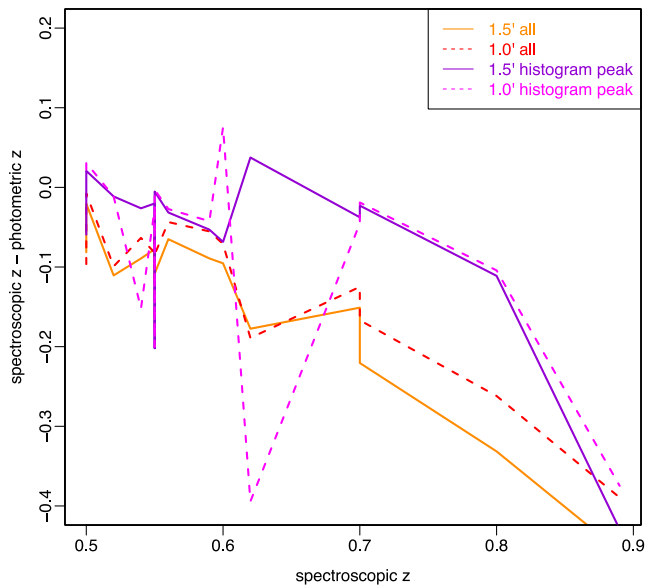


**Figure 4.** The difference between the cluster spectroscopic redshift and the photometric redshift estimates derived from two methods (see Section 6.2.1) applied to SDSS objects with photometric information within 1.5 arcmin of the cluster X-ray centroid (from Piffaretti et al. 2011), in solid lines and within 1 arcmin, in dashed lines. The data points corresponding to each of the selected MCXC clusters (see Section 6.2.1 for details) are joined by lines to depict trends with spectroscopic redshift more clearly. Typical errors on photometric redshift estimates for galaxies in the SDSS data base are  $\approx 0.1$ – $0.15$ . It is clear that, regardless of the method, the photometric redshift estimates from SDSS correlate poorly with the spectroscopic redshift beyond  $z \gtrsim 0.8$ , due to the poor sensitivity in SDSS, though the data are scarce in this regime. On the other hand, there appears to be a reasonable correspondence up to  $z = 0.6$  to within  $\approx 0.15$ .

**Table 7.** Photometric redshift  $z_{\text{phot}}$  estimates for the *Planck*-discovered, CARMA-detected clusters in our sample; note that P351 is not included due to lack of SDSS coverage. Photometric redshifts for objects found in the SDSS data base within 1.5 and 1 arcmin of the CARMA cluster position were used to estimate a photometric redshift for the cluster. We estimated  $z_{\text{phot}}$  in two ways: (1) using the mean photometric redshift for all objects within the radial search (ALL); (2) using the mean photometric redshift of objects within the radial search which fall within the peak bin of the histograms in Appendix G (histogram peak). The average uncertainty in  $z_{\text{phot}}$  for the relevant objects in the SDSS data base is typically between 0.1 and 0.15. We do not quote these errors since they would be an underestimate of the true error in the  $z_{\text{phot}}$  estimate. The  $z_{\text{phot}}$ s in bold are the ones obtained from what was found to be the most reliable method.

Cluster ID	$z_{\text{phot}}$			
	All (1.5 arcmin)	All (1 arcmin)	Histogram peak (1.5 arcmin)	Histogram peak (1 arcmin)
P014	0.38	0.39	<b>0.37</b>	0.36
P086	0.54	0.55	<b>0.66</b>	0.65
P097	0.52	0.51	<b>0.68</b>	0.68
P109	0.48	0.48	<b>0.52</b>	0.38
P170	0.48	0.50	<b>0.53</b>	0.53
P187	0.30	0.31	<b>0.23</b>	0.24
P190	0.46	0.45	<b>0.51</b>	0.51
P205	0.46	0.44	<b>0.40</b>	0.39

**Table 8.** Information on the number of objects in the (all-sky) *WISE* and SDSS data bases within 1.5 arcmin of the CARMA cluster centroid. In the fourth column, *WISE* objects have an SDSS match if an SDSS object is found within 3 arcsec of the *WISE* object. In the last column red *WISE* objects are those objects that satisfy the MIR colour criterion.

Cluster ID	No. of <i>WISE</i> objects	No. of SDSS objects	No. of <i>WISE</i> objects with no SDSS match	No. of red <i>WISE</i> objects with no SDSS match (overdensity arcmin $^{-2}$ )
P014	34	76	16	8 (1.13)
P086	61	64	26	3 (0.42)
P097	62	87	26	9 (1.27)
P109	50	48	26	2 (0.28)
P170	56	70	26	13 (1.84)
P187	43	74	23	1 (0.14)
P190	55	99	15	8 (1.13)
P205	58	94	9	7 (0.99)
P351	44	NA	44	10 (NA)

### 6.3 Photometric redshift summary

(i) **P014:** the redshift estimate for P014 is unclear. The histogram of SDSS  $z_{\text{phot}}$  is one of the least strongly peaked from our sample, peaking at  $z \approx 0.4$ , and the overdensity of red *WISE* objects without an SDSS counterpart is the third largest in our sample ( $\approx 1.1$  arcmin $^{-2}$ ). It does not have an associated known cluster.

(ii) **P086:** the distribution of SDSS  $z_{\text{phot}}$ s has a peak redshift bin around  $z \approx 0.65$  that contains almost 30 galaxies while the next highest count redshift bin is at a much lower- $z$ , between 0.3 and 0.45 with  $\approx 10$  galaxies less. The overdensity of red *WISE* objects with no matching SDSS source is very small  $\approx 0.4$  galaxies arcmin $^{-2}$ . No known cluster is associated with P086. It is therefore likely that the redshift for P086 is around 0.65.

(iii) **P097:** the majority of the SDSS  $z_{\text{phot}}$ s lie in two bins ranging from 0.45 to 0.75, which amount to a large number of objects (56). The overdensity of red *WISE* objects without an SDSS counterpart is the second highest in the sample with  $\approx 1.3$  galaxies arcmin $^{-2}$ . No known cluster lies within the CARMA SZ contours. The significant number of SDSS sources at intermediate redshifts, suggests that this cluster has a redshift of  $\approx 0.6 \pm 0.15$ . We now have spectroscopic data on this cluster which is being processed.

(iv) **P109:** the redshift estimate for P109 is unclear. The SDSS  $z_{\text{phot}}$  histogram for this cluster is almost uniformly distributed, with few counts per bin, always below 12. Yet the number of unmatched red objects in *WISE* is quite small, only  $\approx 0.28$  galaxies arcmin $^{-2}$  as is the overdensity of red objects in *WISE*. This system does not have an associated known cluster.

(v) **P170:** the distribution of SDSS  $z_{\text{phot}}$ s has a distinct, strong peak around  $z \approx 0.53$ , which is in good agreement with the measured photometric redshift of an SDSS-identified cluster candidate system, WHL J085058.7+483003, at  $z_{\text{phot}} = 0.51$  (Wen et al. 2012) lying within the CARMA SZ contours. Though this is the most likely redshift for P170, it does have the largest overdensity of red *WISE* objects without a match in SDSS ( $\approx 1.84$  galaxies arcmin $^{-2}$ ) and the largest red-object overdensity in *WISE* of the entire sample, which suggests it is at  $z \gtrsim 1$ .

(vi) **P187:** the SDSS distribution of  $z_{\text{phot}}$ s has a sharp peak at  $\approx 0.2$ . The centroid for the known cluster Abell 586 (at  $z_{\text{spec}} = 0.17$ ) is only  $\approx 15$  arcsec away from the CARMA SZ peak. We found only two red *WISE* objects without an SDSS counterpart. Hence, P187 is

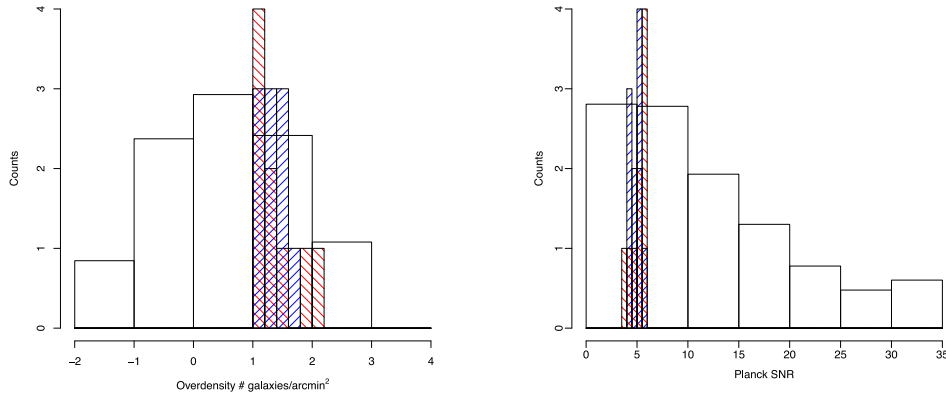


**Figure 5.** Left: histogram of the *WISE* galaxy overdensities centred at the *Planck* cluster candidate position. Overdensities were calculated as the average density of galaxies within a radius of 4.75 arcmin minus the average density in an annulus with inner and outer radii of 4.75 arcmin and 7 arcmin. In white, plotted on a  $\log_{10}$  scale, are the overdensities for all *Planck* clusters. In red, diagonal lines with negative slope, plotted on a linear scale, are the nine clusters with a clear or tentative CARMA-8 detection. While, in blue, diagonal lines with a positive slope, also on a linear scale, are the 10 cluster candidates without a CARMA-8 detection. No clear correlation can be drawn between *WISE* galaxy overdensity and CARMA-8 detectability for our cluster sample. Right: histogram of the *Planck* cluster SNRs. In white, plotted on a  $\log_{10}$  scale, are the SNRs for all *Planck* clusters; in red, diagonal lines with negative slope (in blue, diagonal lines with a positive slope) plotted on a linear scale are shown clusters with a clear/tentative CARMA-8 detection (and without, 10 systems). Out of the 19 clusters in our sample 9 have a CARMA-8 detection and 10 do not. Clusters with an SZ detection in the CARMA-8 tend to have higher SNRs in the *Planck* data.

most definitely Abell 586 and there is no evidence for a line-of-sight cluster at a higher- $z$ .

(vii) **P190:** this system has a clear peak in the histogram of SDSS  $z_{\text{phot}}$ s, peaking at  $\approx 0.51$ . The counts in this ‘peak’ bin ( $\approx 45$ ) are the largest for all our of CARMA-detected clusters. The location of our SZ contours coincide with the position of an identified SDSS cluster candidate with a  $z_{\text{phot}} = 0.49$  (WHL J11608.5+333340; Wen et al. 2012). The overdensity of red *WISE* galaxies with no SDSS match is of  $\approx 1.13$  galaxies arcmin $^{-2}$ . Hence, we expect the redshift of P190 to be  $\approx 0.5$ .

(viii) **P205:** the majority of the SDSS  $z_{\text{phot}}$ s lie in two bins ranging from 0.3 to 0.6, which amount to a large number of objects ( $\approx 80$ ). A known SDSS cluster candidate with  $z_{\text{phot}} = 0.34$  (WHL J113808.9+275431; Wen et al. 2012) is located within the CARMA SZ contours. However, from the relation between the cluster mass and the  $r$ -band SDSS luminosity within  $r_{200}$  from Wen et al. (2012), the  $z = 0.34$  cluster is expected to have  $M_{200} = 0.6 \times 10^{14} M_{\odot}$ . Such a low-mass cluster would not be detectable in our CARMA data. The overdensity of red *WISE* galaxies with no SDSS match is of  $\approx 1$  galaxy arcmin $^{-2}$ . Hence, without much evidence for a higher redshift galaxy overdensity, we expect the redshift of P205 to be 0.34.

(ix) **P351:** we do not estimate a redshift for P351 as there is no SDSS coverage towards this system.

#### 6.4 Improvements to the selection strategy for detecting high redshift, *Planck*-discovered cluster candidates with CARMA

The primary goal of this project was to identify the highest redshift, most massive clusters by cross-correlating the *Planck* SZ-cluster catalogues and *WISE* galaxy catalogues. The two main drivers in the selection of our clusters, which were found to have a large overdensity of sources in the *WISE* early data release, as well as a bright red object satisfying the MIR colour criterion, were:

- (1) the size of the *WISE* overdensity and
- (2) the SNR in the *Planck* data.

In Fig. 5 we investigate if any of these two quantities correlate well with clusters with an SZ detection in the CARMA-8 data. In the left-hand panel we show the histogram for the distribution of *WISE*-object overdensities for all *Planck* cluster candidates, which has a mean value and s.d. of 0.54 and 0.59. Overlaid are histograms of the *WISE* overdensities for cluster candidates in our follow-up sample with and without CARMA SZ detections. The average overdensity (and s.d.) towards CARMA-8-detected systems is 0.95 (0.59), and 0.83 (0.43) for those that were not detected. Hence, the *WISE*-object overdensity centred at the *Planck* position, within a large (4.75 arcmin radius, see Section 2), appears to only be a marginal way of selecting *Planck* candidates that are likely to be detected in a short ( $\approx 5$  h) CARMA-8 observation. Since the overdensity was initially calculated within a very large radius, due to the size of the *Planck* beam, but all but one of our CARMA detections were within 2 arcmin, we re-calculated the *WISE* overdensity within 2 arcmin, see Table 9. Narrowing the overdensity radius changed the over density values to  $1.3 \pm 1$  and  $1.0 \pm 1.1$  for the detected and undetected clusters. Applying the red colour cut corresponding to the previously discussed MIR criterion to the *WISE* galaxies does not preferentially result in detectability (Table 9). It therefore appears that the density of *WISE* galaxies cannot be used as a metric to preferentially detect *Planck* cluster candidates in ground-based SZ follow-up observations.

In the right-hand panel of Fig. 5 the *Planck* SNR has been plotted for all *Planck* cluster candidates and, overlaid, are the *Planck* SNRs for clusters with a CARMA-8 detection and without. Clusters that have been detected in the CARMA-8 data tend to have the highest *Planck* SNRs, as would be expected, showing that *Planck* SNR does correlate well with detectability in our CARMA observations. Out of the clusters in our sample, six do not have a match in the Union catalogue: P031, P049, P052, P264, P097 and P351. These six clusters have *Planck* SNRs ranging from 3.8 to 5.1. There are also six clusters: P028, P057, P090, P121, P134 and P138, that appear in the Union catalogue with SNRs between 4.6 and 5.6 but were not detected in the CARMA-8 data. The next *Planck* SZ catalogue scheduled to be released later in the year and based on the full mission data, will provide a more

**Table 9.** Details on the overdensity of all (and red only) *WISE* objects within 4.75 arcmin or within 2 arcmin of the *Planck* and CARMA SZ-decrement positions. These values were obtained using the ALLWISE data release, while the selection of our targets was made based on the *WISE* early data release. Our sample selection was based on the largest radius, 4.75 arcmin, since only the low-resolution *Planck* data were available at the time. The contribution from field galaxies was estimated within an annulus of 4.75 and 7 arcmin (see Section 2).

Cluster ID	$\delta_{\text{WISE,all}}$ (No. of objects per arcmin <sup>2</sup> )			$\delta_{\text{WISE,red}}$ (No. of objects per arcmin <sup>2</sup> )		
	At <i>Planck</i> <4.75 arcmin	<2 arcmin	At CARMA <2 arcmin	At <i>Planck</i> <4.75 arcmin	<2 arcmin	At CARMA < 2 arcmin
<b>P014</b>	−0.30	0.89	0.25	−0.01	0.44	−0.30
<b>P086</b>	0.24	0.25	1.94	−0.45	−0.83	−0.69
<b>P097</b>	0.87	1.58	1.51	−0.11	−0.54	−0.54
<b>P109</b>	0.99	0.97	0.53	0.05	−0.99	−0.57
<b>P170</b>	0.25	3.59	2.96	−0.10	0.83	0.51
<b>P187</b>	0.95	1.30	1.86	−0.02	0.08	−0.05
<b>P190</b>	1.63	2.32	1.94	0.13	−0.11	−0.13
<b>P205</b>	1.22	1.87	2.29	0.08	0.70	0.20
<b>P351</b>	1.07	0.71	0.99	0.15	0.18	−0.51
P028	0.29	0.35		−0.37	−0.01	
P031	0.89	2.43		0.20	0.21	
P049	1.24	1.47		−0.33	1.05	
P052	0.74	0.30		−0.02	0.38	
P057	1.67	0.74		0.01	0.43	
P090	1.44	0.12		0.04	−0.62	
P121	0.41	1.31		0.10	0.22	
P134	0.68	−0.75		−0.04	0.74	
P138	0.77	2.33		−0.40	−0.55	
P264	0.95	2.63		0.02	0.39	

comprehensive picture of reliability as a function of SNR in the *Planck* catalogues.

## 7 CONCLUSIONS

CARMA 31 GHz data were collected towards 19 candidate clusters identified in *Planck* data, which were selected to have a significant (1–2 galaxies arcmin<sup>−2</sup>) overdensity of objects in the *WISE* early data release and a bright (but fainter than 15.8 mag at 3.4  $\mu\text{m}$ ), red ([3.4]–[4.6] > −0.1 AB mag) object – the putative BCG – within  $\approx 2.5$  arcmin from the *Planck* position. After removal of foreground radio sources identified in the LB CARMA-8 data, we detect eight clear ( $\gtrsim 4.4\sigma$ ) SZ signals – most of which are associated with substantial extended X-ray emission in *ROSAT* – and one tentative signal in the SB CARMA-8 data. The eight clear SZ decrements are, on average, offset from the map centre (and *Planck* position) by  $\approx 1.2$  arcmin and have peak PB-corrected flux densities ranging from −2.1 to −4.2 mJy; the tentative detection towards P014 is offset by  $\approx 160$  arcsec and has a peak flux density of −1.5 mJy.

Out of the 10 *Planck* cluster candidates without a CARMA SZ signal, the likely causes for the lack of a robust detection towards seven are contamination from radio sources and/or a high rms in the CARMA data. For one, P028, while the radio-source environment appears to be benign at 31 GHz, at 1.4 GHz it does not; given the rms of the high-resolution CARMA-8 data towards this system, undetected radio sources could be filling a possible decrement. The CARMA-8 and NVSS data suggest that P090 and P264 should have been detected. We also explore the level of 100  $\mu\text{m}$  ISM contamination to the *Planck* data. Based on this, together with results from CARMA and *ROSAT*, we conclude that, out of the cluster candidates without a CARMA detection, four are likely to

be spurious and three are likely to be real, one of which is P090, as it has compelling, extended X-ray emission in *ROSAT*, comparable to that of Abell 586 (P187), which has a measured SZ mass of  $\approx 5 \times 10^{14} h_{100}^{-1} M_{\odot}$  (AMI Consortium 2012).

We find that, for our sample of objects, a CARMA-8 SZ detection is most likely to be obtained for candidate clusters with a higher SNR in *Planck* but not necessarily for those with a higher value of our estimate of *WISE*-object overdensity.

The high-resolution CARMA-8 data showed that, out of the SZ-detected systems, only three had the putative red BCG lying within the SZ contours. To shed light on the possible photometric redshift of these systems, we produced histograms of the SDSS photometric redshifts of galaxies located within 1.5 arcmin of the CARMA SZ peak. We find that the histograms display a distinctive narrow peak for four systems and a less prominent peak for two more, while one system exhibited an almost uniform distribution and another a bi-modal distribution (SDSS data were missing for the remaining system). The average SDSS photometric redshift for cluster candidates detected in CARMA was  $\approx 0.5$ . To test our methodology, we selected the 17 MCXC clusters with SDSS data, as well as  $M_{500} \geq 2.5 \times 10^{14} M_{\odot}$  and  $z \geq 0.5$  (properties that we expect our sample of cluster candidates to share). We find that, out to  $z \approx 0.6$ , the difference in spectroscopic and photometric redshifts is  $\lesssim 0.15$ , for all but one cluster and that the method fails dramatically beyond  $z \approx 0.84$ , though the data are scarce in this regime.

Given that the evidence suggests that most of our cluster candidates are not  $z > 1$  systems, we investigated the fidelity of the [3.4] – [4.6] > −0.1 (AB mag) colour criterion for selecting such systems. We calculated the overdensity of red objects in *WISE* within 2 arcmin towards MCXC clusters and towards a selection of ACT and SPT-discovered systems at  $z > 0.5$ . We found that, as expected, on average the  $z < 1$  clusters had smaller red-object overdensities than

those at  $z > 1$ . However, we also found that the contamination is high, such that using *WISE* red-object overdensities alone for the selection of  $z > 1$  clusters will likely result in the selection of many  $z < 1$  systems.

## ACKNOWLEDGEMENTS

We thank the staff of the Owens Valley Radio observatory and CARMA for their outstanding support, in particular, we would like to thank John Carpenter. Support for CARMA construction was derived from the Gordon and Betty Moore Foundation, the Kenneth T. and Eileen L. Norris Foundation, the James S. McDonnell Foundation, the Associates of the California Institute of Technology, the University of Chicago, the states of California, Illinois, and Maryland, and the National Science Foundation. Ongoing CARMA development and operations are supported by the National Science Foundation under a cooperative agreement, and by the CARMA partner universities. The *Planck* results used in this study are based on observations obtained with the *Planck* satellite (<http://www.esa.int/Planck>), an ESA science mission with instruments and contributions directly funded by ESA Member States, NASA, and Canada. This publication makes use of data products from the *Wide-field Infrared Survey Explorer*, which is a joint project of the University of California, Los Angeles, and the Jet Propulsion Laboratory/California Institute of Technology, funded by the National Aeronautics and Space Administration. We acknowledge the use of NASA's SkyView facility (<http://skyview.gsfc.nasa.gov>) located at NASA Goddard Space Flight Center. We also wish to thank the referee, Dr Yvette Perrott, for very useful comments on this manuscript.

## REFERENCES

- Abell G. O., Corwin H. G., Jr, Olowin R. P., 1989, *ApJS*, 70, 1  
 Allen S. W., Evrard A. E., Mantz A. B., 2011, *ARA&A*, 49, 409  
 AMI Consortium, 2011, *MNRAS*, 414, L75  
 AMI Consortium, 2012, *MNRAS*, 425, 162  
 Assef R. J. et al., 2013, *ApJ*, 772, 26  
 Bahcall N. A., Fan X., 1998, *ApJ*, 504, 1  
 Bardeen J. M., Bond J. R., Kaiser N., Szalay A. S., 1986, *ApJ*, 304, 15  
 Bonaldi A., Tormen G., Dolag K., Moscardini L., 2007, *MNRAS*, 378, 1248  
 Bond J. R., Myers S. T., 1996, *ApJS*, 103, 1  
 Bond J. R., Kofman L., Pogosyan D., 1996, *Nature*, 380, 603  
 Brodwin M. et al., 2012, *ApJ*, 753, 162  
 Carlstrom J. E., Holder G. P., Reese E. D., 2002, *ARA&A*, 40, 643  
 Carvalho P., Rocha G., Hobson M. P., 2009, *MNRAS*, 393, 681  
 Carvalho P., Rocha G., Hobson M. P., Lasenby A., 2012, *MNRAS*, 427, 1384  
 Gal R. R., de Carvalho R. R., Lopes P. A. A., Djorgovski S. G., Brunner R. J., Mahabal A., Odewahn S. C., 2003, *AJ*, 125, 2064  
 Galametz A. et al., 2012, *ApJ*, 749, 169  
 Gettings D. P. et al., 2012, *ApJ*, 759, L23  
 Hasselfield M. et al., 2013, *J. Cosmol. Astropart. Phys.*, 7, 8  
 Herranz D., Sanz J. L., Hobson M. P., Barreiro R. B., Diego J. M., Martínez-González E., Lasenby A. N., 2002, *MNRAS*, 336, 1057  
 Högbom J. A., 1974, *A&AS*, 15, 417  
 Kay S. T., Peel M. W., Short C. J., Thomas P. A., Young O. E., Battye R. A., Liddle A. R., Pearce F. R., 2012, *MNRAS*, 422, 1999  
 McGlynn T., Scollick K., White N., 1998, in McLean B. J., Golombek D. A., Hayes J. J. E., Payne H. E., eds, *Proc. IAU Symp. 179, New Horizons from Multi-Wavelength Sky Surveys*. Kluwer, Dordrecht, p. 465  
 Marriage T. A. et al., 2011, *ApJ*, 737, 61  
 Melin J.-B., Bartlett J. G., Delabrouille J., 2006, *A&A*, 459, 341  
 Montero-Dorta A. D., Prada F., 2009, *MNRAS*, 399, 1106  
 Motl P. M., Hallman E. J., Burns J. O., Norman M. L., 2005, *ApJ*, 623, L63  
 Muchovej S. et al., 2007, *ApJ*, 663, 708  
 Muchovej S. et al., 2010, *ApJ*, 716, 521  
 Muzzin A., Wilson G., Demarco R., Lidman C., Nantais J., Hoekstra H., Yee H. K. C., Rettura A., 2013, *ApJ*, 767, 39  
 Papovich C., 2008, *ApJ*, 676, 206  
 Perrott Y. C. et al., 2014, *A&A*, preprint ([arXiv:1405.5013](https://arxiv.org/abs/1405.5013))  
 Piffaretti R., Arnaud M., Pratt G. W., Pointecouteau E., Melin J.-B., 2011, *A&A*, 534, A109  
 Planck Collaboration I, 2011a, *A&A*, 536, A1  
 Planck Collaboration VIII, 2011b, *A&A*, 536, A8  
 Planck Collaboration II, 2013a, *A&A*, 550, A128  
 Planck Collaboration XX, 2013b, *A&A*, 571, A20  
 Planck Collaboration XXIX, 2013c, *A&A*, 571, A29  
 Reichardt C. L. et al., 2013, *ApJ*, 763, 127  
 Rettura A. et al., 2014, *ApJ*, preprint ([arXiv:1404.0023](https://arxiv.org/abs/1404.0023))  
 Rykoff E. S. et al., 2014, *ApJ*, 785, 104  
 Sayers J., Czakon N. G., Bridge C., Golwala S. R., Koch P. M., Lin K.-Y., Molnar S. M., Umetsu K., 2012, *ApJ*, 749, L15  
 Shepherd M. C., 1997, in Hunt G., Payne H. E., eds., *ASP Conf. Ser. Vol. 125, Astronomical Data Analysis Software and Systems VI*. Astron. Soc. Pac., San Francisco, p. 77  
 Stern D. et al., 2012, *ApJ*, 753, 30  
 Sunyaev R. A., Zel'dovich Y. B., 1972, *Comments Astrophys. Space Phys.*, 4, 173  
 Tauber J. A. et al., 2010, *A&A*, 520, A1  
 Viana P. T. P., Liddle A. R., 1996, *MNRAS*, 281, 323  
 Voit G. M., 2005, *Rev. Mod. Phys.*, 77, 207  
 Wen Z. L., Han J. L., Liu F. S., 2012, *ApJS*, 199, 34  
 Wenger M. et al., 2000, *A&AS*, 143, 9  
 Williamson R. et al., 2011, *ApJ*, 738, 139  
 Wright E. L. et al., 2010, *AJ*, 140, 1868  
 Zwart J. T. L. et al., 2008, *MNRAS*, 391, 1545

**APPENDIX A: CARMA-8 SB MAPS, WISE MULTICOLOUR IMAGES AND ROSAT MAPS FOR PLANCK CLUSTER CANDIDATES FROM OUR SAMPLE WITHOUT A CARMA SZ DETECTION**

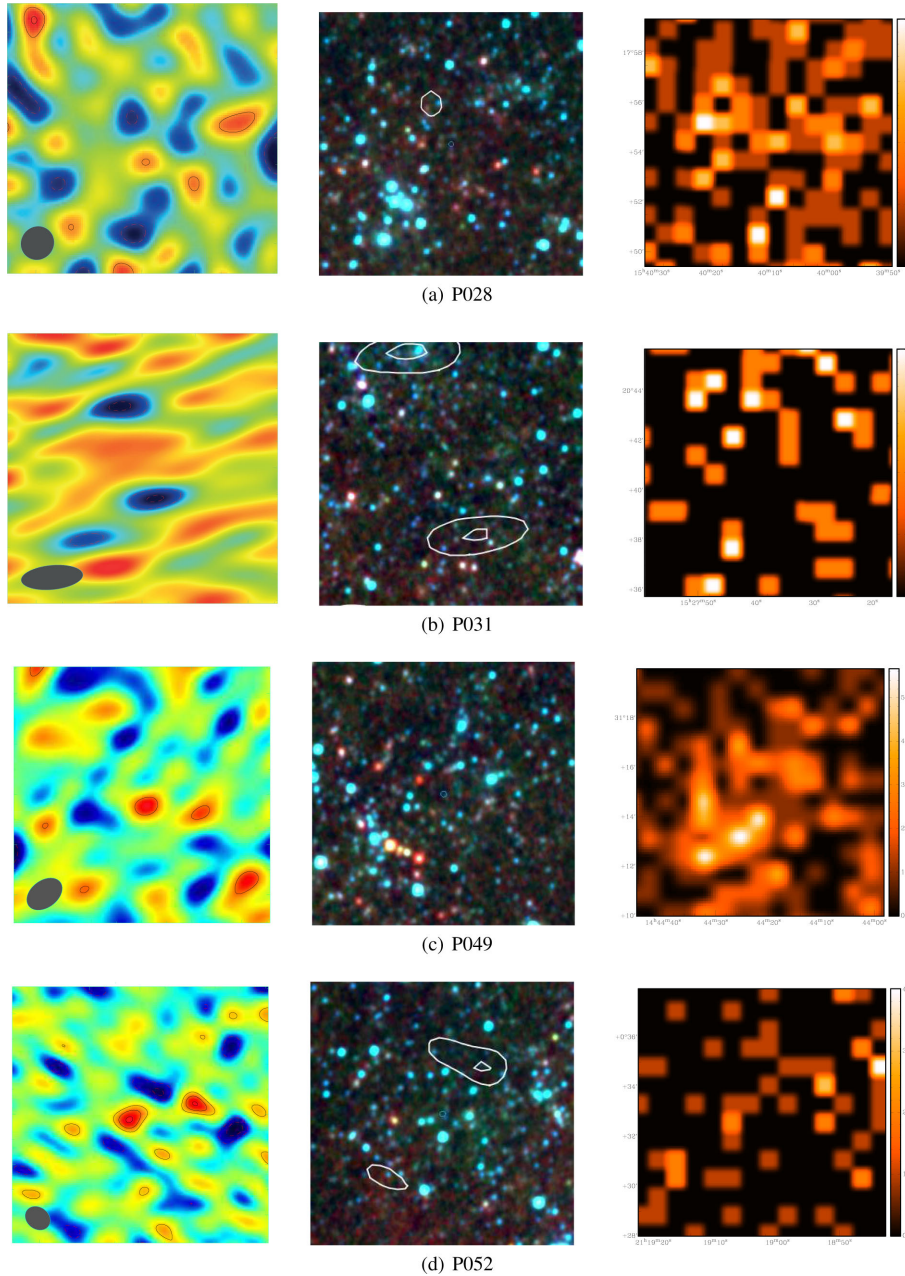


**Figure A1.** CARMA-8, *WISE* and *ROSAT* images for cluster candidates selected in this study without a CARMA-8 SZ detection. The left-hand panel contains the  $1000 \text{ arcsec} \times 1000 \text{ arcsec}$  CLEANED CARMA-8 SB maps centred at the pointing centre after radio-source subtraction, where necessary. This is about twice the *Planck* beam FWHM (7–10 arcmin) relevant for SZ detection. Contours are scaled linearly starting from 2 to  $10\sigma$ , where  $\sigma$  is the noise on the map, in integer multiples. Positive contours are shown in solid, black lines while negative contours are shown in dashed, red lines. The grey ellipse in the bottom-left corner of each map is the synthesized beam, a measure of resolution. No PB correction has been applied. In the middle panel are the *WISE* multicolour 10 arcmin by 10 arcmin plots with the CARMA-8 negative contours overlaid. Channel 1 ( $3.4 \mu\text{m}$ ) is shown in blue, channel 2 ( $4.6 \mu\text{m}$ ) in green and channel 3 ( $12 \mu\text{m}$ ) in red. The blue circles are at the pointing centre of the CARMA observations. The right-hand panel depicts *ROSAT* X-ray images smoothed by a Gaussian function with a radius of 5 arcmin. The images are centred at the CARMA pointing centre, are  $10 \text{ arcmin} \times 10 \text{ arcmin}$  and the pixel unit is counts. The fit files were taken from SkyView (McGlynn, Scollick & White 1998).

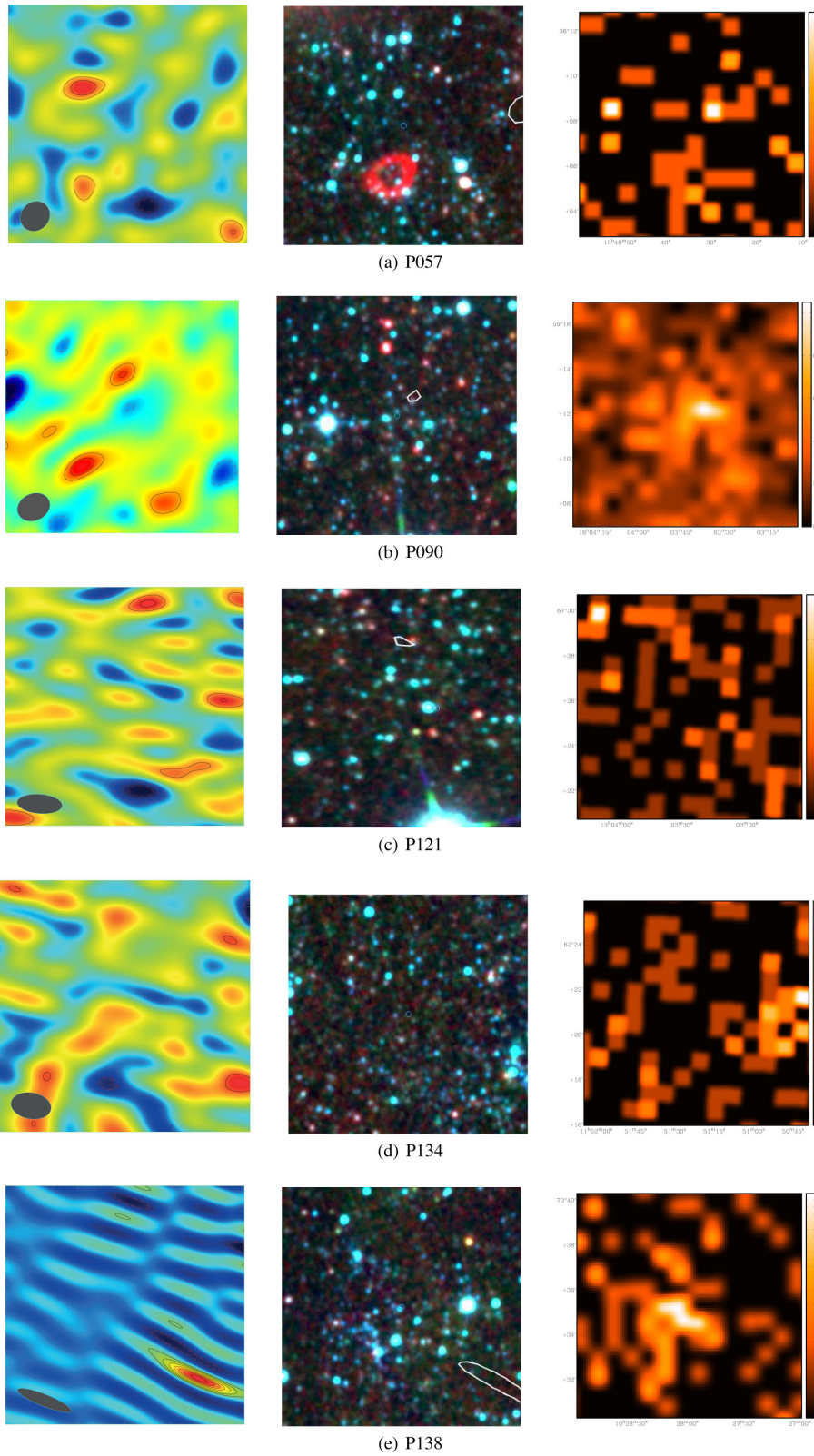
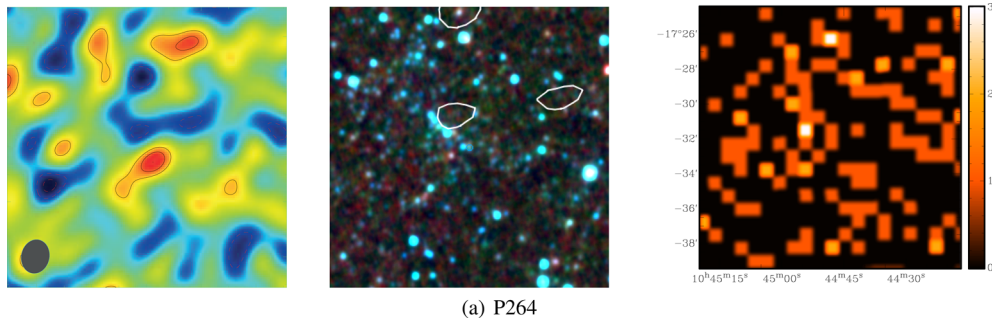


**Figure A1** – *Continued*



(a) P264

Figure A1 – Continued

## APPENDIX B: NOTES ON INDIVIDUAL CARMA-8-DETECTED PLANCK CLUSTER CANDIDATES

**P014:** two radio sources were detected in the LB data, both of which coincide with an NVSS source. There are four more NVSS sources but they are unlikely to contaminate an SZ signal, given their location and 1.4 GHz fitted flux densities. Despite one of the LB-detected radio sources lying  $\approx 2.5$  arcmin away from the map centre with a peak, PB-corrected flux density of 6.3 mJy, the source subtracted LB map is consistent with noise fluctuations, indicating that the removal of these two sources worked well. The SB map after source subtraction has a  $4.2\sigma$  negative feature  $\approx 2.7$  arcmin from the map centre. This is the most significant negative feature on the map and is likely to be a low-SNR SZ detection. This cluster does, however, have the least negative, PB corrected flux density,  $-1.5$  mJy beam $^{-1}$ , which could be due to the 6.3 mJy source located  $\approx 2$  arcmin away partially filling the decrement. The decrement is elongated in the north–south (S) direction with respect to the synthesized beam. In the *Planck* Union catalogue it has an SNR of 4.5. On the other hand, there is no X-ray cluster signal in *ROSAT* towards this system, which would suggest that this is indeed a high-redshift object or, rather, a spurious detection.

**P086:** no radio sources were detected in the LB data and only two sources were identified in NVSS at  $\lesssim 5$  mJy at  $\gtrsim 7$  arcmin. The cluster decrement is clearly detected at the  $5.1\sigma$  level. In the inner, high-SNR regions, the projected SZ signal towards this cluster appears to be close to circular. This system has an SNR of 4.6 in the *Planck* Union catalogue, a peak decrement of  $-3.4 \gtrsim$  Jy beam $^{-1}$  and has substantial X-ray emission, as seen in the *ROSAT* image, Appendix E, whose peak lies within the CARMA-8 SZ contours.

**P097:** no radio sources were detected in the LB data. Six sources were identified in NVSS, none of which coincide with likely low-SNR radio sources in the LB data. The brightest NVSS sources have peak flux densities of  $\approx 16$  mJy and are at least 9 arcmin from the map centre, thus, we do not expect them to contaminate the  $4.4\sigma$  CARMA SZ detection. The detected SZ signal has a highly non-circular, extended shape with a peak flux density of  $-3.0$  mJy beam $^{-1}$ . The *ROSAT* image shows X-ray emission within the CARMA-8 SZ contours with two peaks of  $\approx 4$  counts each. A tentative filament of X-ray emission extends  $\approx 5$  arcmin S with a peak of 4 counts. P097 is not included in the Union catalogue but has an SNR of 4.8 in our analysis of the *Planck* data.

**P109:** one radio source with a peak flux density of 2.6 mJy was detected in the LB data, but it does not correspond to any of the six sources in the NVSS catalogue. The LB-detected radio source is co-

incident with the SZ signal and could be affecting the  $7.3\sigma$  detection, whose peak SZ flux density is  $-4.2$  mJy beam $^{-1}$ . From the maps, the cluster appears to be extended in the north-east and S directions. The *ROSAT* image reveals the presence of X-ray emission, at the level of 3 to 4 counts, that could be associated with the CARMA-8 SZ signal. This X-ray emission extends S for  $\approx 2$  arcmin, where it peaks with 5 counts. P109 is included in the Union catalogue with an SNR of 5.3.

**P170:** there are four identified NVSS radio sources, one of which is located at the position of an LB-detected source. After removing the radio source, the LB map looks noise-like and a clear  $7.3\sigma$  SZ decrement with a peak flux density of  $-3.1$  mJy beam $^{-1}$  is seen in the SB map. The cluster decrement is elongated with respect to the synthesized beam in the north-west direction. In the *ROSAT* images not much X-ray emission can be seen, with a peak of 2 counts lying just outside the edge of the  $2\sigma$  CARMA SZ contour. With a Union SNR of 6.7, this is the cluster in our sample with the highest SNR in the Union catalogue.

**P187:** there is a high density of sources in NVSS towards this cluster candidate with 10 catalogued sources. One of these sources is located next to an LB-detected source that appears to be slightly extended in the LB data. Despite this, the source is removed well from the LB data, which are consistent with noise. A clear  $5.8\sigma$  SZ detection is revealed in the CLEANED SB maps. The decrement is one of the largest in our sample extending over  $\approx 4$  arcmin and branches out in several directions, primarily towards the south-east (SE), suggestive of a dynamically disturbed system. A known cluster, Abell 586, at  $z = 0.171$  lies  $\approx 50$  arcsec away from the map centre. The peak of the X-ray emission towards Abell 586 is offset from the SZ peak in our observations by  $\approx 110$  arcsec, to the south-west (SW). The X-ray image of Abell 586 is circular and compact ( $\approx 1$  arcmin in radius) such that there is only a small overlap between the CARMA and X-ray signals. Abell 586 has been observed at arcminute resolution, at 16 GHz with AMI (AMI Consortium 2012), where it had a peak flux of  $-1.3$  mJy beam $^{-1}$  coincident with the X-ray position and was clearly extended, with signal over  $\approx 8$  arcmin. The AMI SZ signal is fairly circular around a radius of  $\approx 2$  arcmin from the SZ/X-ray peaks, where it is barely resolved, but is distinctly elongated in the SW direction at larger radii. The synthesized beam is approximately circular with a radius of  $\approx 1.5$  arcmin. The higher resolution CARMA data overlap with the AMI signal to the E of the AMI SZ peak. The AMI signal does not show the same SE elongation in the signal in this region as the CARMA data but this difference is likely to be instrumental rather than astrophysical, due to the poorer AMI resolution and the tilt in the CARMA beam. What is interesting is that the SZ signal in the

CARMA data shows no extension in the SW direction, where a large fraction of the AMI SZ flux lies. This ‘missing’ signal from the CARMA data has a measured signal of almost  $-1 \text{ mJy beam}^{-1}$  in the AMI data; since the SZ flux is stronger at 31 GHz than it is at 16 GHz, we would expect to see this signal in the CARMA data at  $\gtrsim 3\sigma$ . The AMI and CARMA SZ peaks are almost equidistant from the map centre, just in a different direction, and, hence, the lack of signal in the SW region should not be due to a sensitivity issue. Most likely, the CARMA-8 data have resolved out part of the signal AMI detects on the larger scales. In the *ROSAT* image there is a distinctive excess of X-ray emission whose peak coincides with the CARMA SZ peak. The X-ray emission drops fast towards the SW, except for a lobe stretching out  $\approx 1$  arcmin, but remains significant towards the SW with 5 counts even beyond the  $2\sigma$  CARMA SZ contour. P187 has an SNR of 6.1 in the *Planck* Union catalogue.

*P190*: there are six NVSS radio sources within 10 arcmin of the map centre, one 41 arcsec away from the map centre with a flux of 9.8 mJy and another offset by 447 arcsec with a flux of 80.8 mJy. No sources are seen in the LB data and, thus, no source subtraction was undertaken. A strong SZ decrement is seen in the SB data at almost  $10\sigma$ , with a peak flux density of  $-3.6 \text{ mJy beam}^{-1}$ . The *ROSAT* image shows some concentrated X-ray emission peaking at  $\approx 4$  counts towards the edge of the CARMA-8 SZ contours. P190 has an SNR of 4.6 in the *Planck* Union catalogue.

*P205*: the SZ decrement is clearly detected towards P205 at  $6.8\sigma$  significance in the CLEANED SB maps. The radio-source environment is not expected to pose a problem to the measured SZ signal: no

sources were detected in the LB data and the 10 NVSS sources are not very bright  $\lesssim 10 \text{ mJy}$  and mostly  $\gtrsim 5$  arcmin away from the map centre. The SZ signal is extended in the NS direction. X-ray counts at the two-photon level can be seen in the *ROSAT* image covering the CARMA-8 SZ contours with a peak of 3 counts towards the edge of the SZ contours. In the *Planck* Union catalogue this system has an SNR of 5.7.

*P351*: one radio source was detected in the LB data  $\approx 4$  arcmin away from the map centre with a flux of 3.3 mJy and thus should not be affecting the cluster decrement. The subtraction of this source worked well leaving a noise-like LB map. The LB-detected source was associated with a 51.7 mJy NVSS source. The remaining seven NVSS sources do not lie on significant positive-flux features in the LB data. The brightest of these sources had a flux of 127.9 mJy and was located 10 arcmin away from the map centre. The LB peak flux density at this location was of  $< 1 \text{ mJy}$ . The peak flux density for this SZ signal was one of the smaller ones for the sample  $-2.1 \text{ mJy beam}^{-1}$  but the detection is significant at  $5.6\sigma$ . Some weak X-ray emission coincident with the CARMA SZ signal is seen in the *ROSAT* image; the X-ray peak, at  $\approx 3$  counts, lies at the edge of the  $2\sigma$  SZ contour. P351 is not included in the Union catalogue and has a low SNR ( $3.8\sigma$ ) in the *Planck* data.

## APPENDIX C: CATALOGUED CLUSTERS AND GALAXY OVERDENSITIES IN THE VICINITY OF OUR OBSERVATIONS

**Table C1.** Registered cluster and cluster candidates that lie within the 4 arcmin of our CARMA-8 map centres. X-ray mass estimates within  $r_{500}$  – the radius at which the mean gas density is 500 times the critical density – ( $M_{X,500}$ ) have been taken from the MCXC catalogue (Piffaretti et al. 2011). Distances are given with respect to the pointing centre of the CARMA-8 observations, unless otherwise stated. For details on the CARMA-8 data towards these clusters see Section 5.  $N_{\text{gals}}$ , the richness estimator, for the WHL clusters is calculated in Wen et al. (2012) within  $r_{200}^a$  and for the other clusters in Gal et al. (2003) within a radius of  $1h^{-1}$  Mpc at the cluster redshift. Redshifts are spectroscopic, unless labelled (phot), in which case they are photometric. Cluster candidates detected in the CARMA-8 data have their cluster ID highlighted in bold font.

Cluster ID	Known cluster	Distance (arcsec)	$z$	$N_{\text{gals}}$	$M_{X,500}$ $\times 10^{14} M_{\odot}$	Comments
P028	Abell 2108 <sup>b</sup>	105	0.09		1.919	Low mass and $z$ – some SZ flux could be resolved out
P028	NSC J154002+175240 <sup>c</sup>	150	0.0789	49.2		Low counts – likely to be a low-mass system
P028	WHL J154000.1+175609 <sup>d</sup>	177	0.39 (phot)	52		Low $z$ – some SZ flux could be resolved out
P049	A1961 <sup>b</sup>	132	0.23		3.532	Low counts – likely to be a low-mass system
P049	WHL J144431.8+311336 <sup>d</sup>	155	0.23 (phot)	103		Ought to be seen yet there is
P049	NSC J144432+311149 <sup>c</sup>	237	0.2334	66.5		no associated decrement in the C8 data
P052	WHL J211849.1+003337 <sup>d</sup>	204	0.28 (phot)	76		Substantial PB attenuation
P057	Abell 2131 <sup>b</sup>	240			69	Substantial PB attenuation.
						Likely to be low-mass system and no X-ray detection.
P057	WHL J154833.7+360536 <sup>d</sup>	138	0.24 (phot)	79		
P121	WHL J130331.7+672638 <sup>d</sup>	60	0.21 (phot)	86		
P134	WHL J115049.1+621948 <sup>d</sup>	237	0.35 (phot)	73		Substantial PB attenuation
<b>P014</b>	WHL J160319.0+031645 <sup>d</sup>	153	0.22 (phot)	114		Not associated with a CARMA decrement.
<b>P086</b>	WHL J151351.9+524960 <sup>d</sup>	199	0.68 (phot)	11		Detected CARMA SZ signal 107.448 arcsec away.
						Not coincident with the CARMA SZ decrement (152 arcsec away). likely to be low mass
<b>P097</b>	WHL J145526.9+585030 <sup>d</sup>	124	0.33 (phot)	22		Not coincident with the CARMA SZ decrement (111 arcsec away). likely to be low mass
<b>P170</b>	WHL J085058.7+483003 <sup>d</sup>	66	0.51 (phot)	33		Coincident with the CARMA SZ detection (34 arcsec away)
<b>P187</b>	Abell 586 <sup>b</sup>	50	0.171		5.197	Coincident with CARMA SZ detection (15 arcsec away)
	WHL JJ073220.3+313801 <sup>d</sup>	48	0.18 (phot)	145		

Table C1 – continued

Cluster ID	Known cluster	Distance (arcsec)	$z$	$N_{\text{gals}}$	$M_{X, 500} \times 10^{14} M_{\odot}$	Comments
<b>P190</b>	WHL J110608.5+333340 <sup>d</sup>	55	0.49 (phot)	73		Coincident with the SZ CARMA detection (21 arcsec away)
<b>P205</b>	WHL J113808.9+275431 <sup>d</sup>	69	0.34 (phot)	12		Coincident with the SZ CARMA detection (15 arcsec away)

<sup>a</sup>Typical  $r_{200}$  in Wen et al. (2012) correspond to scales  $\approx 4\text{--}8$  arcmin.

<sup>b</sup>Reference: Abell, Corwin & Olowin (1989).

<sup>c</sup>Reference: Gal et al. (2003).

<sup>d</sup>Reference: Wen et al. (2012).

## APPENDIX D: WISE MULTICOLOUR PLOTS

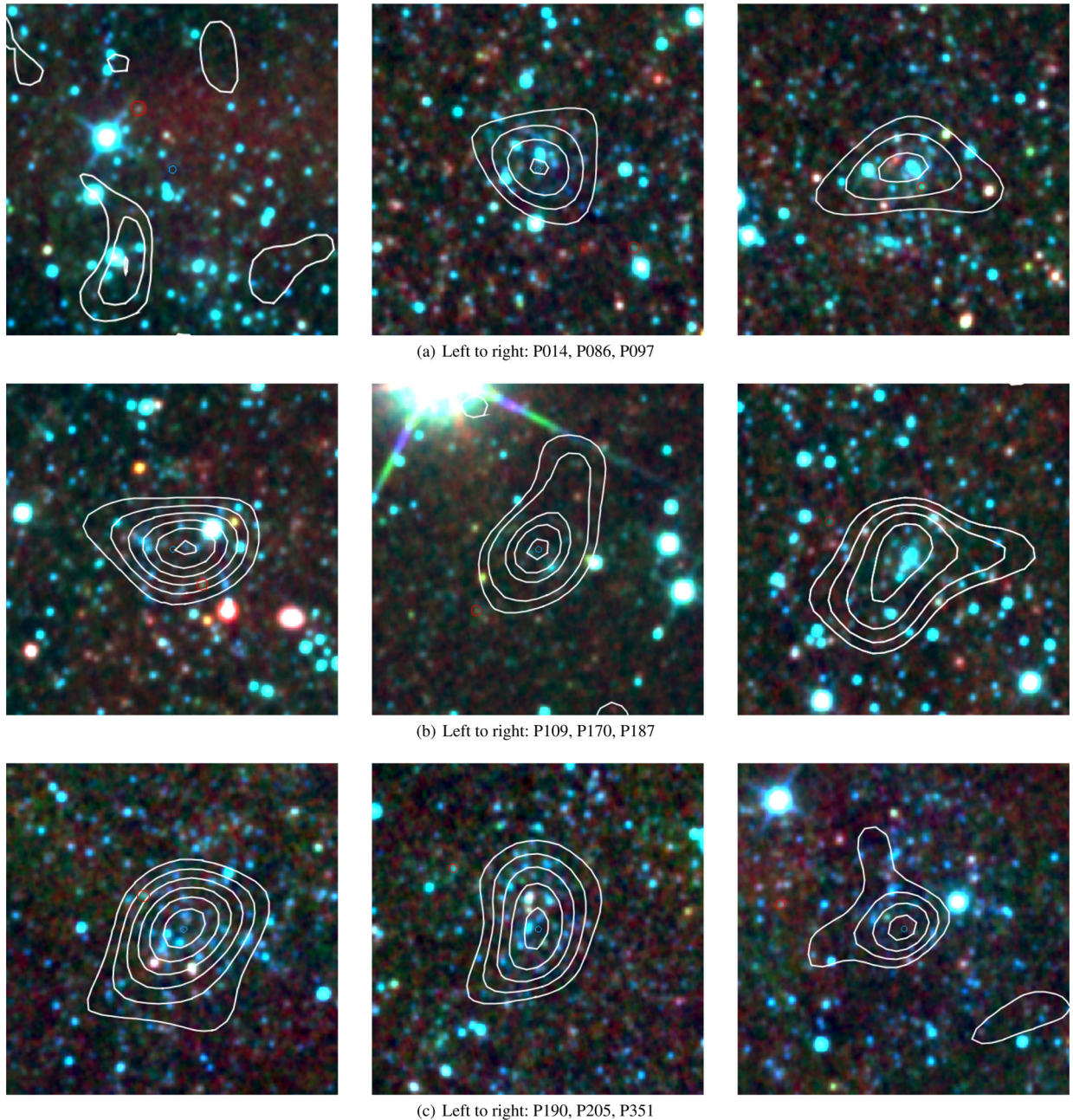


**Figure D1.** *WISE* multicolour plots with the CARMA-8 negative contours overlaid. W1 [3.4  $\mu\text{m}$ ] is shown in blue, W2 [4.6  $\mu\text{m}$ ] in green and W3 [12  $\mu\text{m}$ ] in red. The red circle indicates the position of the putative (red) BCG and the blue circle is at the pointing centre of the CARMA observations.

**APPENDIX E: ROSAT X-RAY IMAGES**

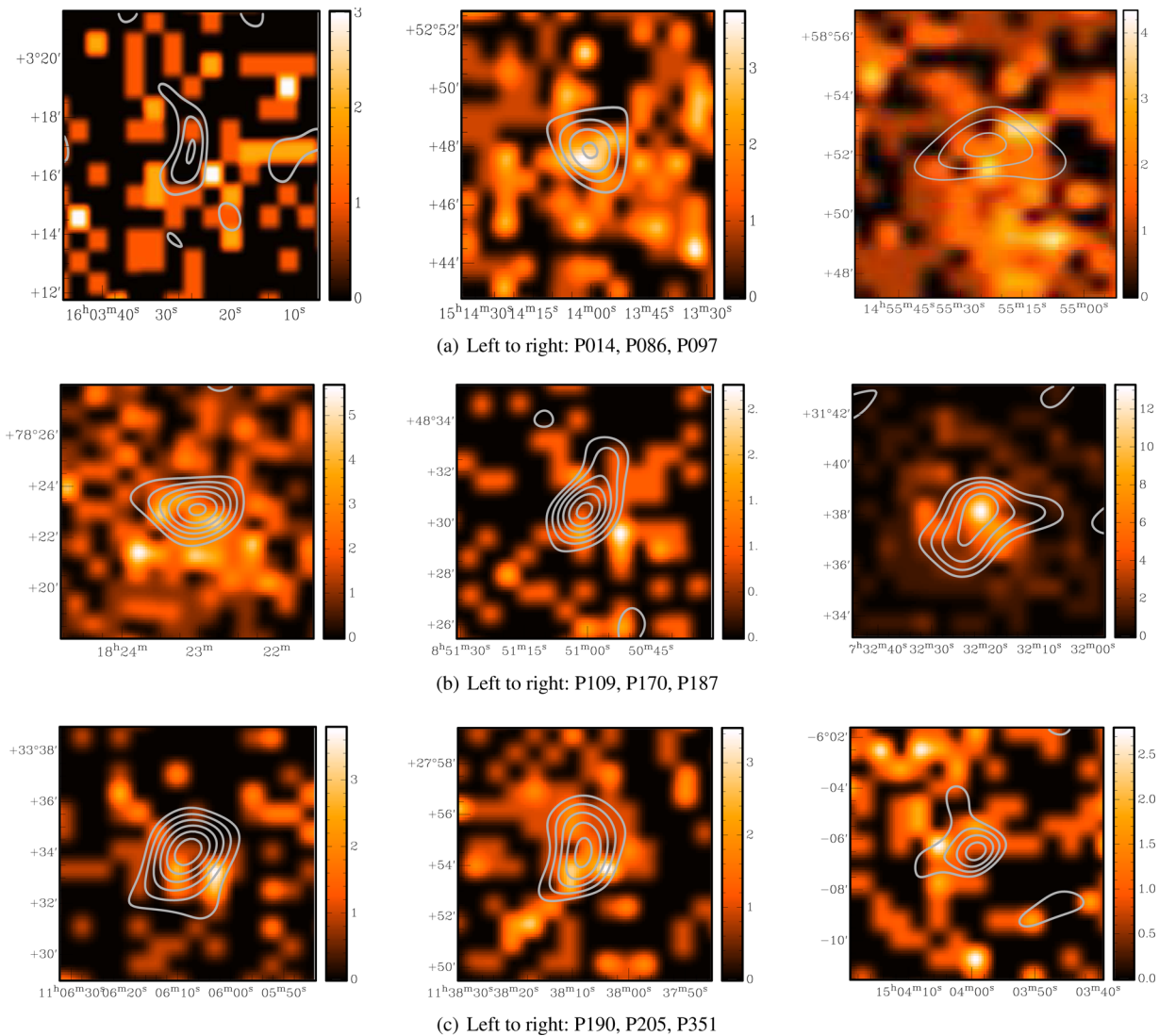


**Figure E1.** ROSAT images for CARMA detections smoothed by a Gaussian function with a radius of 5. The images are centred at the position of the CARMA SZ decrement and are 10 arcmin  $\times$  10 arcmin. The fit files were taken from SkyView (McGlynn et al. 1998).

## APPENDIX F: WISE COLOUR–MAGNITUDE PLOTS

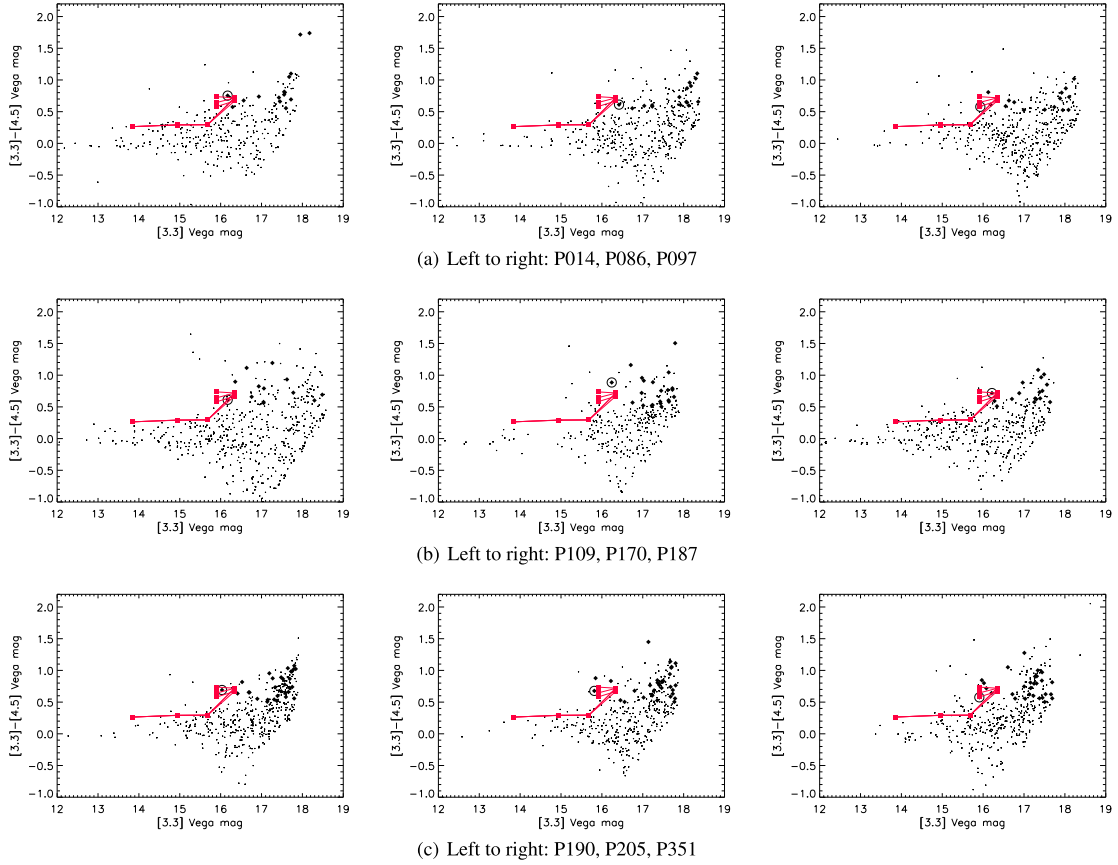


**Figure F1.** The colour–magnitude distribution of *WISE* sources at the location of the CARMA SZ-detected galaxy clusters. The dots show the colour–magnitude relation of the objects corresponding to the overdensity i.e. within 4.75 arcmin of the SZ centroid. The solid black symbols show the red ( $[3.4] - [4.6] > -0.1$  AB mag) objects which are within 2.5 arcmin of the CARMA SZ centroid. The circled object is the brightest galaxy among the red objects and the putative bright cluster galaxy. Also shown are tracks for a passively evolving starburst of mass  $1 \times 10^{12} M_{\odot}$ , and an e-folding time-scale of star formation of 100 Myr with the square symbols marked at redshifts of 3, 2, 1, 0.5 and 0.25. The formation redshift of the burst was 3, 5 or 7. Between redshifts of 1 and 2, the tracks become bluer from the  $k$ -correction due to the shape of the stellar SED around the vicinity of the  $1.6 \mu\text{m}$  bump. Galaxies to the top right of these tracks are likely lower mass starbursts with moderate extinction.

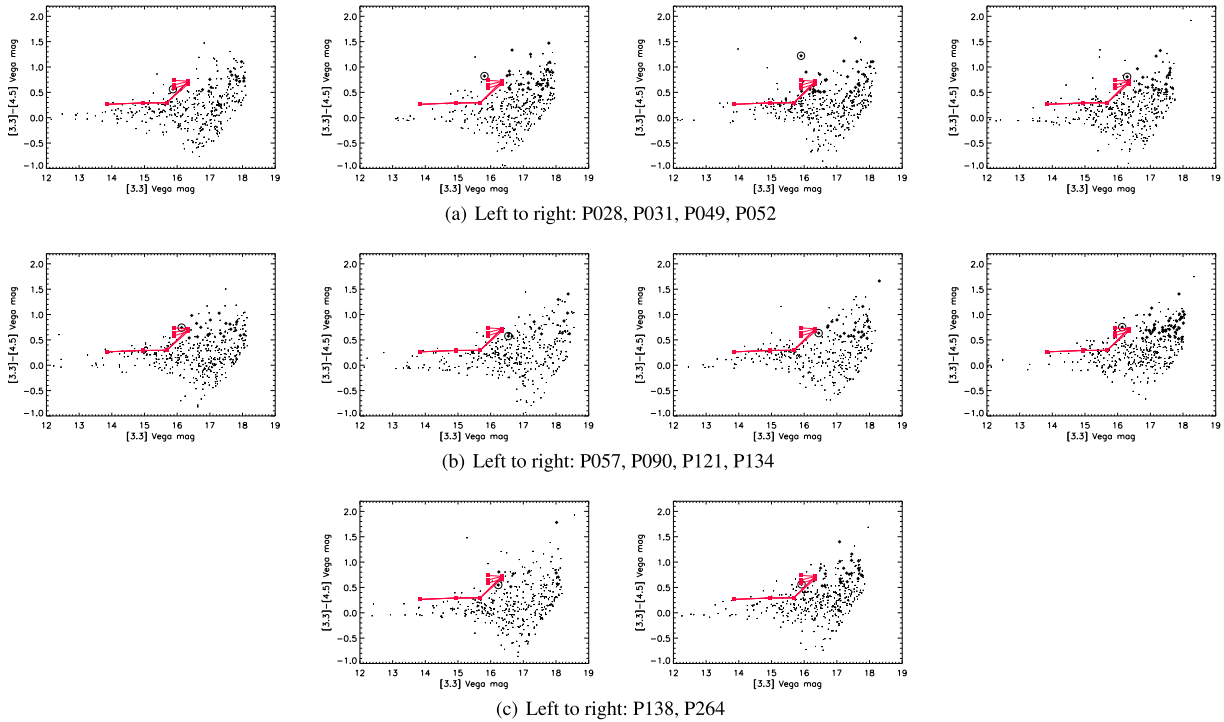


**Figure F2.** Colour–magnitude plots like the ones above but this time for cluster candidates without a CARMA-8 detection and centred at the *Planck* cluster position.

## APPENDIX G: SDSS PHOTOMETRIC REDSHIFTS

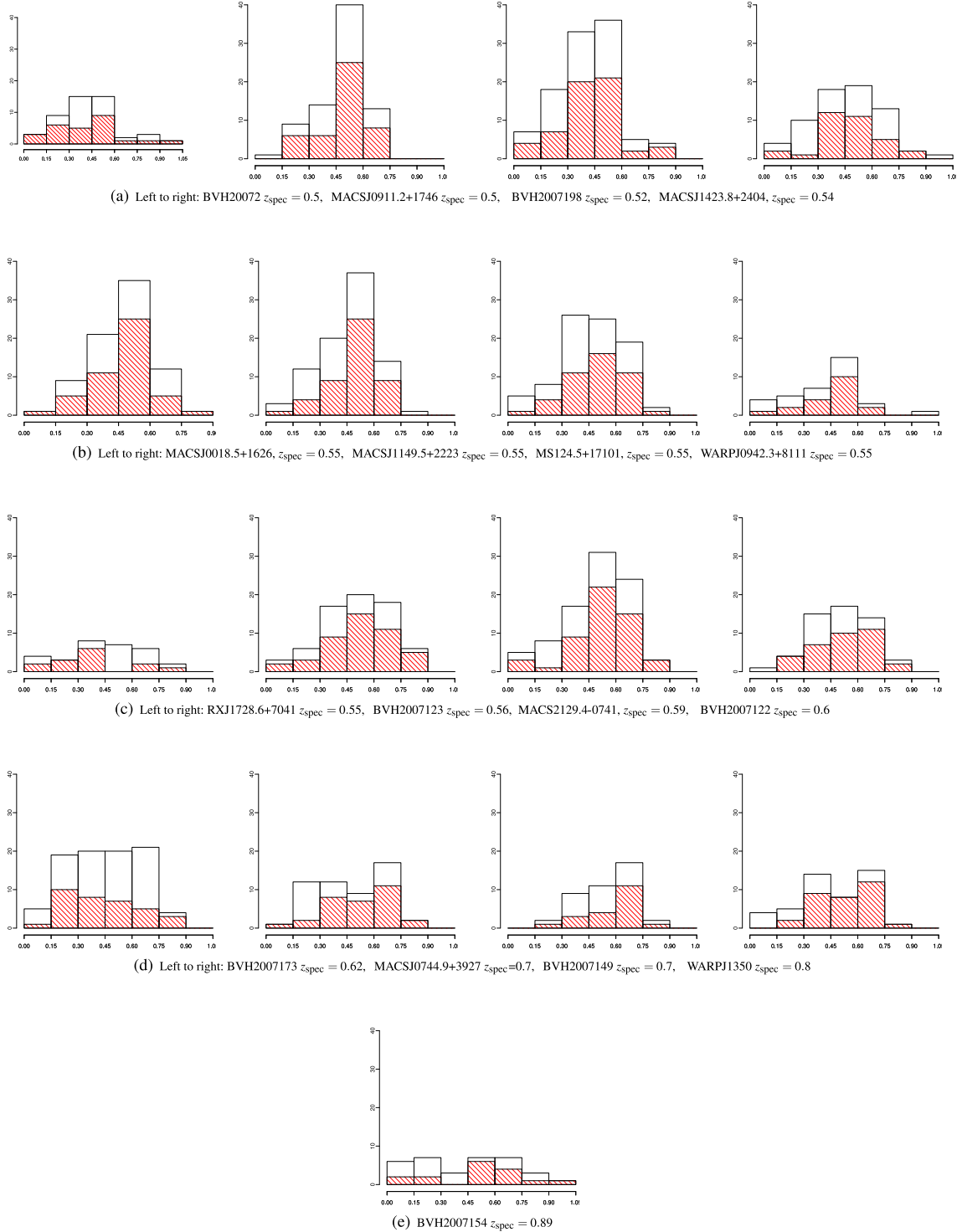


**Figure G1.** Histograms of the photometric redshifts of SDSS objects lying within 1.5 arcmin (white) and 1.0 arcmin (red, diagonal lines) of the MCXC cluster position (Piffaretti et al. 2011). Each plot is labelled with the cluster name and the spectroscopic redshift estimates given in the MCXC catalogue. The  $N_{\text{gals}}$  derived from this work need not match those from Wen et al. (2012) for various reasons, including the search radius, which, for Wen et al., is typically  $\approx 4$ –8 arcmin and the filters applied by Wen et al. for quality purposes e.g. they require small photometric errors.

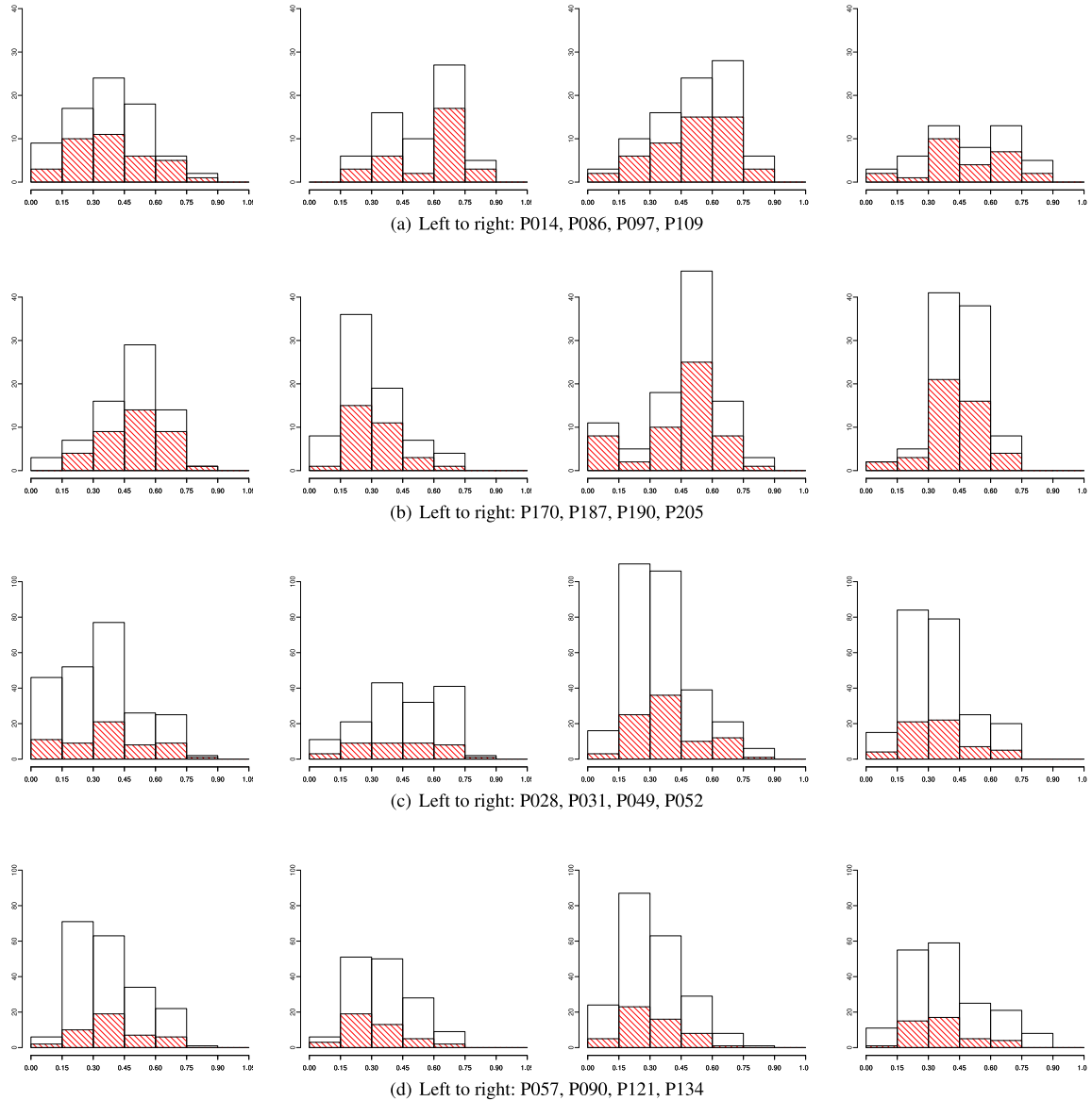


**Figure G2.** Histograms of the photometric redshifts of SDSS objects lying within 1.5 arcmin (white) and 1.0 arcmin (red, diagonal lines) of the CARMA-derived cluster position for CARMA-detected systems (first two rows) and within 3.0 arcmin (white) and 1.5 arcmin (red, diagonal lines) of the *Planck* position for cluster candidates without an SZ CARMA detection (last two rows). Each plot is labelled with the shorthand ID name. The data suggest that many of the CARMA-8 non-detections are likely at  $z \sim 0.3$ .

This paper has been typeset from a  $\text{\TeX}/\text{\LaTeX}$  file prepared by the author.